ADVANCING EARTH AND SPACE SCIENCE

JAMES | Journal of Advances in Modeling Earth Systems®

RESEARCH ARTICLE
10.1029/2022MS003078

Special Section:
Advances in scaling and modeling of land-atmosphere interactions

Key Points:

- We describe a new tool for investigating canopy-chemistry-turbulence interactions at isoprene-dominated deciduous forests
- Spatial segregation of air masses in the canopy can bias reaction rates assuming well-mixed conditions by up to −48% to +23%
- There is stronger segregation for many reactions when soil NO emissions reflect the upper bound of observed values for temperate forests

Supporting Information:

Supporting Information may be found in the online version of this article.

Correspondence to:
O. E. Clifton,
olivia.e.clifton@nasa.gov

Citation:
Clifton, O. E., Patton, E. G., Wang, S., Barth, M., Orlando, J., & Schwantes, R. H. (2022). Large eddy simulation for investigating coupled forest canopy and turbulence influences on atmospheric chemistry. *Journal of Advances in Modeling Earth Systems*, *14*, e2022MS003078. https://doi.org/10.1029/2022MS003078

Received 11 MAR 2022
Accepted 20 SEP 2022

Large Eddy Simulation for Investigating Coupled Forest Canopy and Turbulence Influences on Atmospheric Chemistry

Olivia E. Clifton[1,2], **Edward G. Patton**[1], **Siyuan Wang**[3,4], **Mary Barth**[1], **John Orlando**[1], and **Rebecca H. Schwantes**[3,4]

[1]National Center for Atmospheric Research, Boulder, CO, USA, [2]Now at NASA Goddard Institute for Space Studies, New York, NY, USA, [3]Cooperative Institute for Research in Environmental Sciences, University of Colorado Boulder, Boulder, CO, USA, [4]NOAA Chemical Sciences Laboratory, Boulder, CO, USA

Abstract Exchanges of reactive gases between forests and the atmosphere influence tropospheric chemistry, climate, and ecosystems. Chemistry inside canopies can alter these exchanges yet understanding of the chemistry and processes influencing the chemistry is incomplete. Previous work prioritizes complex chemical mechanisms over micrometeorology in the multilayer models of forests used to understand in-canopy chemistry and its impacts. Instead, here we use a new simplified chemical mechanism and resolve turbulence in a multilayer canopy model. Specifically, we describe a new version of the National Center for Atmospheric Research large eddy simulation (LES) coupled to both a multilayer canopy model and a chemical mechanism. The mechanism has 41 reactions and 19 gases for ozone, NO_x (=NO + NO_2), HO_x (=OH + HO_2), and isoprene chemistry. We evaluate the mechanism against two more complex mechanisms using box modeling. We configure the LES for a temperate deciduous forest and summer midday weak-wind buoyancy-forced conditions. The multilayer canopy model necessitates estimates of reactant sources and sinks at each canopy level, and thus we describe multilayer parameterizations for dry deposition and biogenic emissions. For the first time with an LES coupled to both a multilayer canopy and chemistry, we demonstrate variability in chemical reactions due to turbulence-induced segregation of reactants inside and just above the canopy. For the cases examined here, in-canopy segregation alters reaction rates that only consider well-mixed conditions by up to −48% to +23%. For many reactions, segregation is stronger when soil NO emissions reflect the upper bound of observed values for temperate forests.

Plain Language Summary The atmospheric boundary layer (ABL) (the part of the atmosphere closest to the earth) organizes itself into structured air motions that vertically transport momentum, energy, and reactive gases toward and away from the Earth's surface. This is important because the Earth's surface provides sources and sinks of momentum, energy, and reactive gases. The presence of forest canopies can alter the structured air motions in the ABL, and the structured air motions influence canopy sources and sinks of momentum, energy, and reactive gases, implying a coupling between the canopy and the structured air motions that may influence atmospheric chemistry. We describe a computer model with very high spatial resolution that can be used to examine the impact of the relationship between these organized motions, the canopy, and chemistry. Other computer models that have been used to examine atmospheric chemistry in canopies only consider the average effect of the organized motions. We show that the organized motions can influence chemical reactions rates substantially in the canopy, rendering the model described here an important tool for interpreting observations and advancing understanding of the impact on atmospheric chemistry important for climate and air pollution.

1. Introduction

Land-atmosphere exchanges of reactive gases play an important role in our earth system, influencing tropospheric chemistry, climate, and ecosystems (Arneth et al., 2011; Barth et al., 2005; Farmer & Riches, 2020; Fowler et al., 2009; He et al., 2021; Steiner, 2020). For example, emissions of biogenic volatile organic compounds (BVOCs) from vegetation contribute to the formation of tropospheric ozone and secondary organic aerosol, both air pollutants and short-lived climate forcers (Fehsenfeld et al., 1992; Fiore et al., 2012; Hallquist et al., 2009; Henze & Seinfeld, 2006; Trainer et al., 1987). Air pollution and the atmospheric oxidizing capacity also depend on NO_x (=NO + NO_2) (Crutzen, 1974, 1979; Levy, 1971), which has a soil source and a vegetation sink (Delaria et al., 2018; Jacob & Bakwin, 1991; Wang et al., 2020; Yienger & Levy, 1995). A key but overlooked component of forest-atmosphere chemical exchanges is turbulence.

Generally, organized eddy structures comprise turbulence in the atmospheric boundary layer (ABL), with their size and character changing with driving forces (e.g., Moeng & Sullivan, 1994; Weckwerth et al., 1997). Inside and just above forest canopies, turbulence is unique. Near canopy top, the mean wind profile has a hydrodynamically unstable inflection point due to vegetation absorbing momentum through its depth. ABL-scale turbulence brings high-momentum air to the canopy top, producing shear-driven canopy-scale eddies (i.e., sweeps and ejections) distinct from the background flow (Finnigan et al., 2009; Gao et al., 1989, 1992; Raupach et al., 1996). In unstable conditions, buoyant plumes emanating from the ground and canopy also influence exchange between canopy layers and aloft (e.g., Brunet, 2020; Dupont & Patton, 2012; Patton et al., 2016).

Turbulence influences forest-atmosphere chemical exchanges in several ways. For example, turbulence transports reactive gases out of canopies, allowing compounds emitted by canopy elements or produced within canopy air spaces to influence tropospheric chemistry at local-to-global scales. Turbulence also transports gases into the canopy, allowing gases in the ABL to meet their fate via in-canopy ambient chemical loss and dry deposition to canopy surfaces. Organized structures in turbulence can lead to spatial variations in reactant abundances and thus the physical separation of reactants ("segregation"). Because organization in turbulence can happen on timescales important for atmospheric chemistry, segregation can cause reaction rates to speed up or slow down relative to rates that assume well-mixed conditions (Kim et al., 2016; Krol et al., 2000; Patton et al., 2001; Schumann, 1989; Sykes et al., 1992, 1994). Segregation may be particularly important in the canopy where there are distinct sources and sinks of reactants that vary in space and time (Edburg et al., 2012; Patton et al., 2001).

Despite the key role of turbulence in forest-atmosphere chemical exchanges, models almost always only consider the influence of turbulence in a bulk sense. Thus, turbulent transport is often not accurately represented, and the impact of segregation cannot be quantified. While multilayer models of vegetation canopies (hereinafter, MLMs) have been coupled to complex chemical mechanisms to examine exchanges of reactive gases and the related in-canopy chemistry for many years (e.g., Ashworth et al., 2015; Bryan et al., 2012; Forkel et al., 2006; Ganzeveld et al., 2002; Wei et al., 2021; Wolfe & Thornton, 2011), chemistry MLMs have yet to be coupled to turbulence-resolving large eddy simulation (LES) with one exception (Fuentes et al., 2022). LES is a powerful tool for investigating turbulence including within and above canopies (e.g., Kanda & Hino, 1994; Ma & Liu, 2019; Shaw & Schumann, 1992; Su et al., 1998) yet can be computationally expensive.

The National Center for Atmospheric Research LES is coupled to an MLM (hereinafter, NCAR-LES-MLM) such that vertical changes in light attenuation, canopy and soil sources and sinks of moisture and heat, the canopy-imposed sink of momentum, and canopy drag all influence turbulent flow (Patton et al., 2016). We document a new version of the NCAR-LES-MLM coupled to a simplified chemical mechanism (hereinafter, NCAR-LES-MLM-CHEM) that represents ozone, NO_x, HO_x (=OH + HO_2), and isoprene chemistry. Our model prioritizes resolution of turbulence over complex chemistry, in contrast to the current suite of tools used to investigate chemical exchanges that prioritize complex chemistry. To our knowledge, reactant segregation in and above the canopy has never been demonstrated using an LES coupled to a chemistry MLM through canopy drag and interactive sources and sinks of heat, water vapor, and reactants. Specifically, unique to the NCAR-LES-MLM-CHEM is dynamic and spatially varying leaf-level emission and dry deposition of reactants, as well as water vapor and heat sources. In Fuentes et al. (2022), which also does not investigate segregation, sources and sinks of heat and water vapor are forced with observed fluxes, and emissions of isoprene are imposed with an offline vertical distribution.

We configure the NCAR-LES-MLM-CHEM for midday summer weak-wind buoyancy-forced conditions at a temperate deciduous forest. Deciduous forests are key sources of isoprene, globally the largest emitted BVOC and non-methane volatile organic compound (Guenther et al., 1995, 2012). Our simulated forest, with its relatively high ambient humidity and soil moisture, dense isoprene-emitting deciduous trees, idealizes a southeast US forest. The southeast US has been a focus in atmospheric chemistry research due to field campaigns in summer 2013 that aimed to understand climate and pollution relevant low-NO_x isoprene chemistry (e.g., Carlton et al., 2018; Mao et al., 2018). Previous work used airborne observations over the southeast US during summer 2013 to constrain segregation between OH and isoprene in the ABL (Kaser et al., 2015). Here we leverage the NCAR-LES-MLM-CHEM to probe how segregation impacts first-generation isoprene chemistry. We focus on inside and just above the canopy where segregation may be particularly important due to unique turbulence and

Table 1
Simulated Conditions by the NCAR-LES-MLM-CHEM

Case	z_i (m)	u_* (m s^{-1})	$\overline{w'\theta_v'}$ (m K s^{-1})	w_* (m s^{-1})	w_m (m s^{-1})
Low soil NO	402	0.22	0.14	1.22	1.23
High soil NO	402	0.22	0.14	1.22	1.23

Note. All variables are horizontally and temporally averaged. All variables except the ABL height (z_i) are from canopy top. u_* is friction velocity. $\overline{w'\theta_v'}$ is the buoyancy flux. w_* is the Deardorff convective velocity scale. w_m is a scaling velocity combining shear and buoyancy forcing.

interactive reactant sources and sinks. We also investigate segregation in the context of uncertainty in soil NO emissions. For example, southeast U.S. soil NO emissions are relatively unconstrained but expected to be an important contribution to regional NO$_x$ and air pollution (Romer et al., 2018; Travis et al., 2016), and the few observations of soil NO emissions for temperate deciduous forests vary by three orders of magnitude (Thornton et al., 1997; Valente & Thornton, 1993; Williams & Fehsenfeld, 1991).

2. Model Description and Evaluation

2.1. NCAR Multilayer Canopy Large Eddy Simulation

The NCAR-LES (e.g., Moeng, 1984; Moeng & Wyngaard, 1988; Sullivan et al., 1996; Sullivan & Patton, 2011) solves the three-dimensional time-dependent spatially filtered fluid motion equations under the Boussinesq approximation. A discrete Poisson equation for pressure enforces incompressibility. In Section 2.1, we describe the NCAR-LES-MLM, and in Section 2.2 we introduce the NCAR-LES-MLM-CHEM. Note that the NCAR-LES has been coupled to chemistry before but without a vertically resolved and coupled forest canopy (hereinafter, NCAR-LES-CHEM).

In the NCAR-LES-MLM (Patton et al., 2016), terms representing pressure and viscous drag as well as scalar sources and sinks are produced by spatially filtering the conservation equations in the presence of canopy elements (Patton & Finnigan, 2013). Boundary conditions in the horizontal directions are periodic. A rough-wall boundary condition is imposed at the surface with Monin Obukhov Similarity Theory (MOST) determining transfer between the lowest grid point and the ground. Sub-filter scale (SFS) momentum and scalar fluxes are parameterized with down-gradient diffusion assumptions and estimated SFS turbulent kinetic energy (TKE) (Deardorff, 1980; Shaw & Patton, 2003). We assume that all scalars mix similarly to heat at SFSs.

The physical model configuration follows Clifton and Patton (2021). In brief, the simulation domain is 2,048 m in both horizontal directions and 1,024 m in the vertical direction. The spatial resolution is 2 m × 2 m × 2 m. The horizontal dimensions are at least fivefold larger than the ABL height (z_i; Table 1) to minimize the influence of periodic boundary conditions on ABL-scale turbulent structures.

The NCAR-LES-MLM simulates flow interacting with a forest with horizontally homogeneous properties. The specified vertical leaf area density (LAD) profile has a maximum in the upper canopy and a relatively sparse understory, typical for a deciduous tree (Figure 1). The canopy height (h) is 20 m. The NCAR-LES-MLM represents multiple canopy layers in each 2 m × 2 m vertical column in the 2,048 m × 2,048 m horizontal domain. In each grid cell inside the canopy, the MLM simulates processes like leaf energy balance and photosynthesis for sunlit and shaded leaves in response to the LES forcing and provides leaf-level water and heat sources back to the LES at each time step. Canopy drag occurs primarily through pressure forces and varies spatially with LAD and instantaneous local wind speed (Patton et al., 2016).

We prescribe the vertical distribution of sunlit versus shaded leaves (Figure 1) using Beer's Law for which incoming direct radiation differs based on LAD and solar zenith angle (θ) (e.g., Monteith & Unsworth, 1990; Moon et al., 2020). At a given height (z), the sunlit fraction (f_sun) is:

$$f_\mathrm{sun} = e^{-\Omega \frac{G}{\cos\theta} \int_0^z \mathrm{LAD}(z)\,\mathrm{d}z} \tag{1}$$

The variable θ is the solar zenith angle in radians (0.317), the parameter G relates to leaf orientation (0.5), and the parameter Ω is the clumping index (0.85).

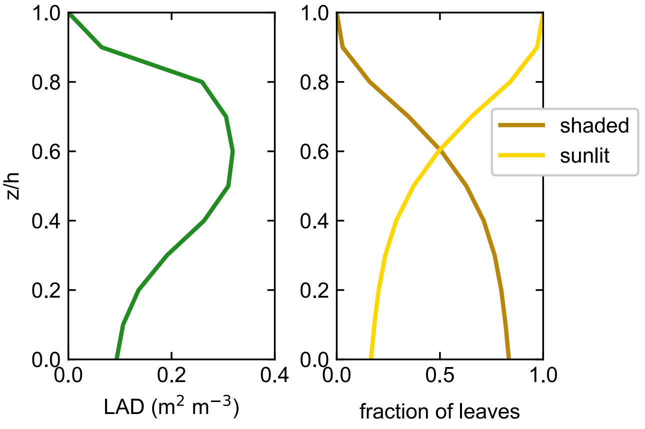

Figure 1. Vertical profiles of leaf area density (LAD) and the fraction of sunlit versus shaded leaves (and canopy air space) from the ground to canopy height (h).

Each vertical column has a 1-m deep soil layer resolved at four levels, and there is a set of roots accessing the soil at every horizontal grid point. Initial soil moisture and temperature conditions are from a 2-year High-Resolution

Land Data Assimilation System simulation (Chen et al., 2007; Patton et al., 2016) to ensure that the initial soil conditions are in equilibrium with the atmosphere.

We prescribe initial vertical profiles of specific humidity, virtual potential temperature, and streamwise wind. The streamwise geostrophic wind is 1 m s^{-1} and the initial vertical profile of the streamwise wind is set to the streamwise geostrophic wind. Initial virtual potential temperature has a 0.08 K m^{-1} gradient spanning 100 m centered on the initial ABL height (400 m) and a 0.003 K m^{-1} gradient in the free troposphere (FT; Sullivan & Patton, 2011). Incoming solar radiation is 847 W m^{-2}. The initial specific humidity is 18 g kg^{-1} in the ABL and 1 g kg^{-1} in the FT.

To initiate turbulence, divergence-free fluctuations are added to the initial horizontal velocity field over the five vertical grid points spanning canopy top (Patton et al., 2016). We discard model results before w_m, a velocity scale incorporating shear and buoyancy forces (Moeng & Sullivan, 1994), becomes constant at canopy top. We then average results over five turnover times ($=z_i/w_m$; Table 1) corresponding to the largest and slowest eddies in the domain. Our simulations, excluding spin up, are each 27 min. The time step varies but averages 0.32 s.

Unless stated otherwise, all quantities reported can be assumed to be averaged horizontally and temporally. We only use overbars in fluxes or covariances, or when the emphasis is needed to understand a quantity; in these cases, the overbars represent horizontal averages, and the primes represent deviations from the horizontal average. Time averaging happens after horizontal averaging. Because all variables are averaged in time unless stated otherwise, we do not include notation denoting this averaging.

Although our model domain extends up into the FT, the focus of this paper is the vicinity of the canopy, strictly speaking from the ground to $3h$.

2.2. Chemistry

2.2.1. New Simplified Chemical Mechanism

Due the computational expense of the NCAR-LES-MLM-CHEM, we employ a simplified gas phase chemical mechanism that simulates the features of tropospheric chemistry involving ozone, isoprene, NO_x and HO_x over deciduous forests. The mechanism has 19 gases (Table 2) and 41 reactions (Table 3) and is designed to represent first-generation isoprene chemistry and similar to Wang et al. (2021). The mechanism is based on Su et al. (2016). Reaction kinetics are updated to reflect the Jet Propulsion Laboratory (JPL; Burkholder et al., 2015) or the International Union of Pure and Applied Chemistry (IUPAC; Atkinson et al., 2004, 2006) databases. The isoprene oxidation is updated based on MOZART T1 (Emmons et al., 2020). We include a simplified representation for the isomerization of the organic peroxy radical (RO_2) from OH reaction with isoprene to form an isoprene-derived hydroperoxy aldehyde (HPALD), which is lumped with isoprene hydroxy aldehydes (HYDRALD). Isomerization of RO_2 is important for HO_x recycling (Crounse et al., 2011). Due to mechanism design, later-generation isoprene chemistry may not be as well represented.

The NCAR-LES-MLM-CHEM uses the Kinetic PreProcessor (KPP; Damian et al., 2002; Sandu & Sander, 2006) to connect the specified chemical mechanism to a Rosenbrock solver for solving the stiff set of ordinary differential equations. Though the version of the NCAR-LES-CHEM with KPP was reported in Lenschow et al. (2016) with a three-reaction mechanism, we emphasize that using KPP and the Rosenbrock solver is an update from other NCAR-LES-CHEM studies (e.g., Kim et al., 2012; Li, Barth, et al., 2016; Li, Su, et al., 2016; Li et al., 2017; Vilà-Guerau de Arellano et al., 2005), allowing the user to easily change chemical mechanisms and employ a highly accurate conservative solver.

We initialize the NCAR-LES-MLM-CHEM with ABL and FT mixing ratios (Table 2) from an NCAR-LES-CHEM simulation for the Southeast Atmosphere Study (SAS) campaign without the resolved canopy at 12:00 Central Standard Time (CST) that started at 6:00 CST (the chemistry was reinitialized to observed values at 08:00 CST). Our NCAR-LES-MLM-CHEM spin up is 1,108 s, reflecting the time it takes the turbulence to develop and reach equilibrium with the forcing. During this transition, ABL-averaged reactant mixing ratios reveal unphysical fluctuations (e.g., see the first hundreds of s in Figure S1 in Supporting Information S1). However, there is likely no effect of the fluctuations on the spatial distribution of the reactants during the production part of the simulation. For example, because time averaging begins 358 s (~6 min) after the final fluctuation in the ABL-averaged reactant mixing ratios, and the turnover time for ABL-size eddies is ~325 s during production, any effect of

Table 2

The Gaseous Species Used in the Chemical Mechanism, the Properties of Each Species Needed for Dry Deposition Estimates, and Their Initial Mixing Ratios in the Atmospheric Boundary Layer (ABL) and Free Troposphere (FT)

Chemical species	Molecular weights (g mol^{-1})	Reactivity f_0 (unitless)	Solubility H^{eff} (M atm^{-1})	Initial mixing ratios (ppb)
OH	17.01	1.0	3.90×10^1	0.584×10^{-4} (ABL)
				0.193×10^{-3} (FT)
HO_2	33.01	0.1	6.90×10^2	0.026 (ABL)
				0.021 (FT)
O_3	48.00	1.0	1.03×10^{-2}	33.66 (ABL)
				37.84 (FT)
H_2O_2	34.01	1.0	8.70×10^4	2.49 (ABL)
				1.23 (FT)
CO	28.01	0.0	9.81×10^{-4}	105.53 (ABL)
				90.27 (FT)
NO	30.01	0.0	1.92×10^{-3}	0.031 (ABL)
				0.012 (FT)
NO_2	46.01	0.1	1.20×10^{-2}	0.067 (ABL)
				0.018 (FT)
NO_3	62.00	1.0	3.80×10^{-2}	0.491×10^{-5} (ABL)
				0.129×10^{-5} (FT)
N_2O_5	108.01	0.1	2.14	0.272×10^{-3} (ABL)
				0.146×10^{-4} (FT)
CH_4	16.04	0.0	1.41×10^{-3}	1,831.36 (ABL)
				1,803.33 (FT)
CH_3O_2	47.03	1.0	2.38	0.009 (ABL)
				0.014 (FT)
HCHO	30.03	1.0	3.23×10^3	2.40 (ABL)
				0.491 (FT)
ISOP	68.11	0.0	3.45×10^{-2}	2.82 (ABL)
				0.109×10^{-3} (FT)
$ISOPAO_2$	117.12	1.0	2.38	0.020 (ABL)
				0.436×10^{-5} (FT)
$ISOPBO_2$	117.12	1.0	2.38	0.012 (ABL)
				0.277×10^{-5} (FT)
ISOPOOH	118.13	1.0	3.50×10^6	0.952 (ABL)
				0.007 (FT)
[HYDRALD + HPALD]	108.11	1.0	1.70×10^5	0.550 (ABL)
				0.002 (FT)
XO_2	149.12	1.0	1.00×10^{11}	0.003 (ABL)
				0.957×10^{-4} (FT)
[MVK + MACR]	70.09	1.0	23.75	1.550 (ABL)
				0.194 (FT)

Note. Values in columns (2)–(3) are from Schwantes et al. (2020) or CESM2.2 except values for $ISOPAO_2$ and $ISOPBO_2$, for which we use CH_3O_2 values, and XO_2 for which we assume very high solubility and reactivity. Brackets around species added together denote species lumped as one in our model. XO_2 is an RO_2 formed oxidation of [HYDRALD + HPALD] and ISOPOOH (Table 3; Emmons et al., 2010).

Table 3
The Reactants, Products, and Reaction Coefficients of the Reactions in the Chemical Mechanism

Reactants	Products	Rate coefficient ($[\text{molecules cm}^{-3}]^{-(n-1)}\ \text{s}^{-1}$)
O_3	2 OH	$K_{H_2O} = 1.63 \times 10^{-10}\ [H_2O]\ e^{60/T}$ $K_{N_2} = 2.15 \times 10^{-11}\ 0.79\ [M]\ e^{110/T}$ $K_{O_2} = 3.30 \times 10^{-11} 0.21\ [M]\ e^{55/T}$ $j_{O(^1D)} = 4.551 \times 10^{-5}$ $K_{H_2O} \frac{j_{O(^1D)}}{K_{H_2O}+K_{N_2}+K_{O_2}}$
NO_2	$NO + O_3$	$j_{NO_2} = 1.144 \times 10^{-2}$
HCHO	$2\ HO_2 + CO$	$j_{HCHO,r} = 3.669 \times 10^{-5}$
HCHO	CO	$j_{HCHO,m} = 5.352 \times 10^{-5}$
$OH + HO_2$	H_2O	$4.8 \times 10^{-11} e^{250/T}$
$OH + O_3$	HO_2	$1.70 \times 10^{-12} e^{-940/T}$
$HO_2 + HO_2$	H_2O_2	$\left(2.3 \times 10^{-13} e^{600/T} + 1.7 \times 10^{-33}\ [M]\ e^{1{,}000/T}\right)\left(1.0 + 1.4 \times 10^{-21}\ [H_2O]\ e^{2{,}200/T}\right)$
$HO_2 + O_3$	OH	$2.03 \times 10^{-16} e^{\frac{693}{T}} \left(\frac{T}{300}\right)^{4.57}$
$NO + O_3$	NO_2	$1.4 \times 10^{-12} e^{-1{,}310/T}$
$NO_2 + OH$		$\frac{1.80{\times}10^{-30}\left(\frac{300}{T}\right)^3[M]}{1+\frac{1.80{\times}10^{-30}\left(\frac{300}{T}\right)^3[M]}{2.80{\times}10^{-11}}} 0.6^{1/1+\log_{10}\left(1.80{\times}10^{-30}\ (300/T)^3[M]/2.80{\times}10^{-11}\right)^2}$
$NO_2 + O_3$	NO_3	$1.4 \times 10^{-13} e^{-2{,}470/T}$
$NO + HO_2$	$NO_2 + OH$	$3.50 \times 10^{-12} e^{270/T}$
$NO_2 + NO_3$	N_2O_5	$\frac{2.40{\times}10^{-30}\left(\frac{300}{T}\right)^3[M]}{1+\frac{2.40{\times}10^{-30}\left(\frac{300}{T}\right)^3[M]}{1.60{\times}10^{-12}\left(\frac{300}{T}\right)^{-0.1}}} 0.6^{1/1+\log_{10}\left(2.40{\times}10^{-30}(300/T)^3[M]/1.60{\times}10^{-12}(300/T)^{-0.1}\right)^2}$
$NO + NO_3$	$NO_2 + NO_2$	$1.8 \times 10^{-11} e^{\frac{110}{T}}$
$HO_2 + NO_3$	$OH + NO_2$	4.0×10^{-12}
$N_2O_5 + M$	$NO_2 + NO_3$	$\frac{1.8{\times}10^{-30}\left(\frac{300}{T}\right)^3[M]}{1+\frac{1.8{\times}10^{-30}\left(\frac{300}{T}\right)^3[M]}{2.8{\times}10^{-11}}} 0.6^{1/\left(1+\log_{10}\left(1.8{\times}10^{-30}(300/T)^3[M]/2.8{\times}10^{-11}\right)\right)} 1.724 \times 10^{26}\ e^{-10840/T}/[M]$
N_2O_5		$2.5 \times 10^{-22}\ [H_2O]$
NO_3	$0.11\ NO + 0.89\ NO_2 + 0.89\ O_3$	$j_{NO_3,o} = 2.591 \times 10^{-2} + 2.051 \times 10^{-1}$
$CH_3O_2 + NO$	$HCHO + 0.99\ NO_2 + HO_2$	$2.80 \times 10^{-12} e^{300/T}$
$CH_3O_2 + HO_2$		$4.10 \times 10^{-13} e^{750/T}$
$CO + OH$	HO_2	$1.5 \times 10^{-13}\ \left(1 + 6 \times 10^{-7}\ k_b[M]\,T\right)$
$CH_4 + OH$	CH_3O_2	$2.45 \times 10^{-12} e^{-1{,}775.0/T}$
$HCHO + OH$	$HO_2 + CO$	$5.50 \times 10^{-12} e^{125.0/T}$
$ISOP + OH$	$0.6\ ISOPAO_2 + 0.4\ ISOPBO_2$	$2.54 \times 10^{-11} e^{410.0/T}$

Table 3
Continued

Reactants	Products	Rate coefficient ([molecules cm^{-3}]$^{-(n-1)}$ s^{-1})
$ISOPAO_2 + CH_3O_2$	$HO_2 + 1.5\ HCHO + 0.75\ [MVK + MACR]$	$5.0 \times 10^{-13} e^{400.0/T}$
$ISOPAO_2 + HO_2$	ISOPOOH	$8.0 \times 10^{-13} e^{700.0/T}$
$ISOPAO_2 + NO$	$0.9\ NO_2 + 0.9\ [MVK + MACR] + 0.9\ HCHO + 0.9\ HO_2 + 0.9\ CO$	$4.4 \times 10^{-12} e^{180.0/T}$
$ISOPBO_2 + CH_3O_2$	$HO_2 + 0.75\ HCHO + 0.75\ [HYDRALD + HPALD]$	$5.0 \times 10^{-13} e^{400.0/T}$
$ISOPBO_2 + HO_2$	ISOPOOH	$8.0 \times 10^{-13} e^{700.0/T}$
$ISOPBO_2$	$[HYDRALD + HPALD] + HO_2$	$1.6 \times 10^{+9} e^{-8300.0/T}$
$ISOPBO_2 + NO$	$0.87\ [HYDRALD + HPALD] + 0.9\ NO_2 + 0.97\ HO_2 + 0.15\ CO + 0.1\ HCHO$	$4.4 \times 10^{-12} e^{180.0/T}$
ISOPOOH + OH	$0.4\ XO_2 + 0.6\ OH$	$1.52 \times 10^{-11} e^{200.0/T}$
ISOPOOH	$0.69\ [MVK + MACR] + 0.69\ HCHO + HO_2$	$j_{ISOPOOH} = 6.457 \times 10^{-6}$
[HYDRALD + HPALD] + OH	XO_2	$1.86 \times 10^{-11} e^{175.0/T}$
[HYDRALD + HPALD]	$OH + HO_2$	$0.004\ j_{NO_2}$
$XO_2 + HO_2$		$8.0 \times 10^{-13} e^{700.0/T}$
$XO_2 + NO$	$0.9\ NO_2 + HO_2 + 0.25\ CO + 0.25\ HCHO$	$2.7 \times 10^{-12} e^{360.0/T}$
[MVK + MACR] + OH	$HO_2 + HCHO + 1.5\ CH_3O_2$	2.4×10^{-11}
$ISOP + O_3$	$0.785\ HCHO + 0.29\ H_2O_2 + 0.363\ CO + 0.125\ HO_2 + 0.205\ OH + 0.675\ [MVK + MACR] + 0.181\ CH_3O_2$	$1.03 \times 10^{-14} e^{-1995.0/T}$
$ISOP + NO_3$		$3.15 \times 10^{-12} e^{-450.0/T}$
H_2O_2	2 OH	$j_{H_2O_2} = 8.499 \times 10^{-6}$

Note. The parameter n is the number of reactants in the chemical reaction; T is air temperature in K; j_X is photolysis rate for species X (values given are not scaled by fraction of sunlight within the canopy); [M] is the third-body concentration (concentration of air used in molecules cm^{-3}); k_b is the Boltzmann constant (1.38×10^{-16} kJ K^{-1}). Brackets around species added together denote species lumped as one in our model.

spin up on the distributions has been mixed. Because kinks during spin up may affect mean mixing ratios for species with lifetimes longer than a few minutes, we report the ABL-averaged mixing ratios in Figure S1 in Supporting Information S1.

Corresponding to the solar radiation at 12:00 CST (847 W m^{-2}), photolysis rates are estimated offline with the NCAR Tropospheric UV and Visible Radiation Model (TUV) 5.0 for clear sky conditions. We scale the estimated photolysis rates using the observed versus estimated photolysis frequency for NO_2 (Table 3). The scaled photolysis rates are fed into the NCAR-LES-MLM-CHEM; they do not vary with time for our short simulations. Aside from inside the canopy, the photolysis rates do not vary vertically. The photolysis rates applied within the canopy are scaled by the fraction of sunlit air space (Figure 1). Our assumption is that the fraction of sunlit canopy air space is the same as the fraction of sunlit leaves, common in chemistry MLMs (e.g., Gao et al., 1993; Moon et al., 2020).

Table 4
Box Model Conditions

Condition	Value
Solar zenith angle	18°
Temperature	301 K
Relative humidity	80%
Pressure	101,325 Pa
CH_4	1,831 ppb
CO	106 ppb
NO	0.1 ppb (clean), 2.5 ppb (polluted)
HCHO	2.0 ppb
H_2O_2	1.9 ppb
Isoprene	8 ppb
O_3	30 ppb

Note. Reactant mixing ratios reflect initial conditions. Other reactants are initialized at 0 ppb.

2.2.2. Box Modeling

We evaluate the performance of the simplified chemical mechanism using a zero-dimensional photochemical box model (Wang & Pratt, 2017; Wang et al., 2019), which solves the ordinary differential equations using the Backwards Differentiation Formula (also known as the Gear approach; Brown et al., 1989). We compare the time evolution of reactants in our simplified mechanism, the MOZART T1 mechanism (151 gases and 287 reactions; Emmons et al., 2020) and the isoprene mechanism in MCM version 3.3.1 (610 gases and 1,945 reactions; Jenkin et al., 2015). MCM 3.3.1 (hereinafter, MCM) is a near-explicit mechanism widely considered as a benchmark, whereas MOZART T1 (hereinafter, T1) is widely employed in chemical transport modeling.

We test the three mechanisms under "clean" and "polluted" scenarios (Table 4). The clean scenario reflects the lowest mean NO in the vicinity of the canopy across our NCAR-LES-MLM-CHEM simulations and the polluted scenario reflects the highest. In all box-model simulations, photolysis frequencies are calculated using the parameterization in MCM; photolysis frequencies calculated with the solar zenith angle value listed in Table 4 are used (the same solar zenith angle as in the NCAR-LES-MLM-CHEM). The temperature and relative humidity used reflect mean conditions in the vicinity of the canopy in the NCAR-LES-MLM-CHEM simulations.

Although the initial chemical conditions for our NCAR-LES-MLM-CHEM simulations arise from an NCAR-LES-CHEM simulation that has been running for a couple of hours, we integrate the chemical evolution forward in time in the NCAR-LES-MLM-CHEM for no longer than 1 hr. We thus examine the three mechanisms with the box modeling, respectively, over 3 hr (1 hour of which we consider as spin up). In general, the box-model results demonstrate that NO_x and ozone as well as the first-generation isoprene chemistry are well represented by our mechanism.

We start describing the box-model results for the polluted scenario because simplified mechanisms likely work best at higher NO_x given that then peroxy radicals react exclusively with NO. For the polluted scenario, our mechanism overestimates OH and HO_2 relative to T1 and MCM (Figure 2). For HO_2, the overestimate is strongest in the second hour and then declines, agreeing with T1 and MCM at the end of the third hour. OH/HO_2 is overestimated relative to T1 and MCM, implying too rapid HO_x cycling. Isoprene rapidly decays to negligible levels. Our mechanism overestimates HCHO with the largest overestimate in the second hour and underestimates [MVK + MACR]. Our mechanism captures isoprene peroxy radicals (ISOP-RO_2) simulated by MCM and that ISOP-RO_2 fate is dominated by reaction with NO. Our mechanism also agrees with T1 and MCM that loss via reaction with HO_2 is second in importance, with the importance increasing with time (and the importance of reaction with NO decreasing in time).

For the clean scenario, our mechanism underestimates OH relative to MCM but agrees with T1 (Figure 3). Our mechanism underestimates HO_2, with a weaker underestimate relative to T1 than MCM. The bias in OH and HO_2 between MCM and our mechanism increases with time. Likely our mechanism underestimates HO_x recycling from the RO_2 isomerization pathway (and thus important at low NO) (Jenkin et al., 2015; Wennberg et al., 2018)

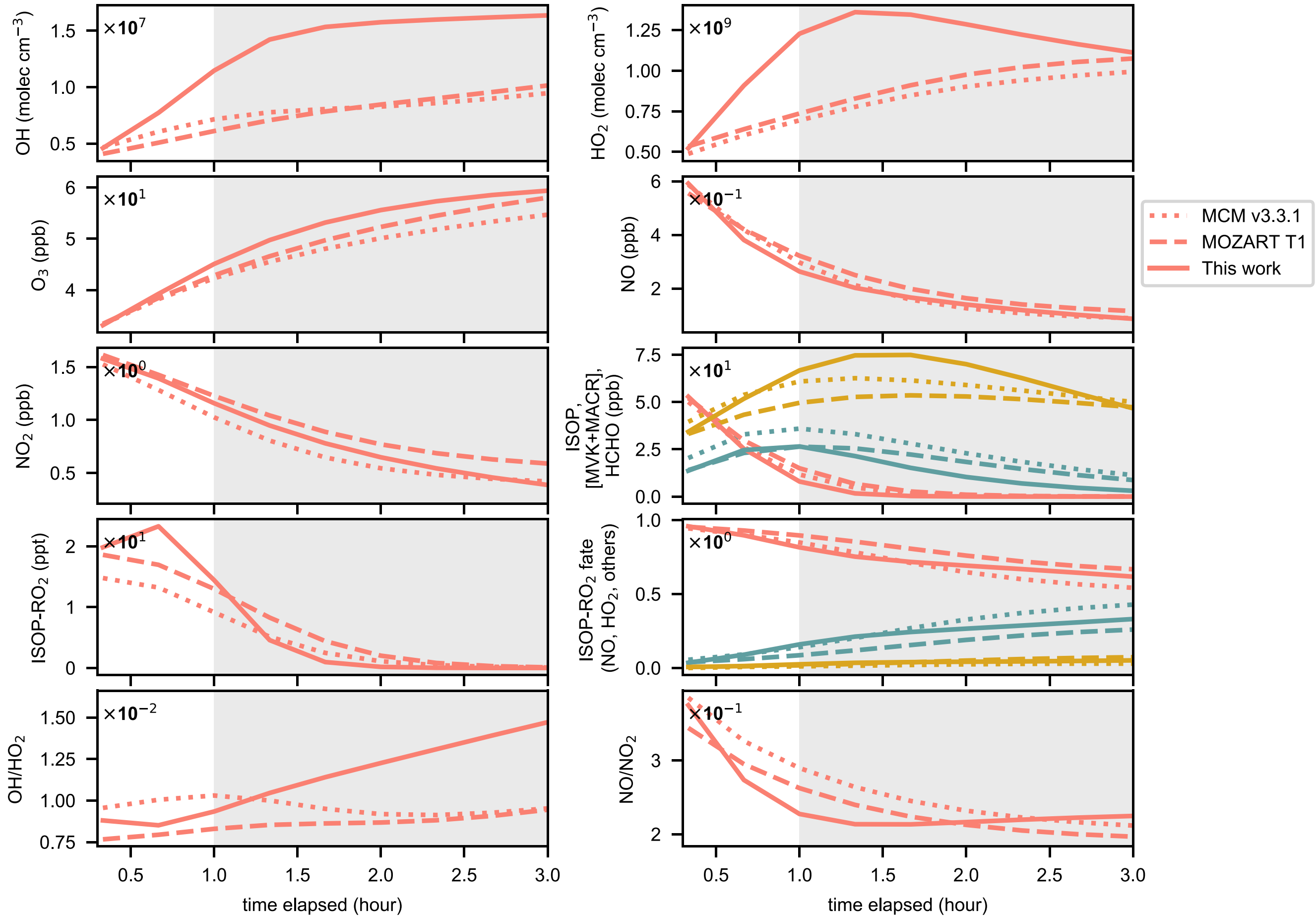

Figure 2. Chemical evolution from box-model simulations of the different chemical mechanisms as a function of time since the simulation start for polluted conditions. For plots with multiple quantities, the first quantity listed on the *y*-axis label is orange, the second is teal, and the third is gold. The first hour is dictated by initial conditions and a few reactions and does not represent the full behavior of the mechanisms so we focus on the final 2 hr, highlighted in gray.

included in MCM, but not in T1 or our mechanism. Nonetheless, even complex mechanisms, including MCM, struggle to capture HO_x recycling and disagree with respect to HO_x production under low-NO_x high-isoprene conditions because the chemistry is complex and not well constrained (Bates & Jacob, 2019; Schwantes et al., 2020; Wennberg et al., 2018). For our mechanism, OH/HO_2 is larger than T1 but smaller than MCM, implying too slow HO_x cycling. In response to low OH in our mechanism relative to MCM, isoprene is overestimated relative to MCM. The similarity in OH between our mechanism and T1 leads to similar isoprene. There is agreement across the mechanisms in [MVK + MACR] and HCHO. Our mechanism overestimates ISOP-RO_2 (the overestimate is larger relative to MCM than T1) but captures that ISOP-RO_2 fate is dominated by reaction with HO_2. Compared to MCM, our mechanism (and T1) slightly underestimates ISOP-RO_2 fate by reaction with HO_2. Likely the difference follows slower reaction rates in T1 and our mechanism versus MCM (factor of 1.9 at 298 K). Our mechanism agrees with T1 and MCM that reaction with NO is second in importance in terms of ISOP-RO_2 fate in the first 2 hours, but then loss via other reactions become more important.

2.3. Biogenic Emissions

2.3.1. Leaves

There are only biogenic emissions of isoprene from leaves in our model. Leaf-level emissions of isoprene are parameterized at each vertical layer of the canopy. We leverage the Model of Emissions of Gases and Aerosols

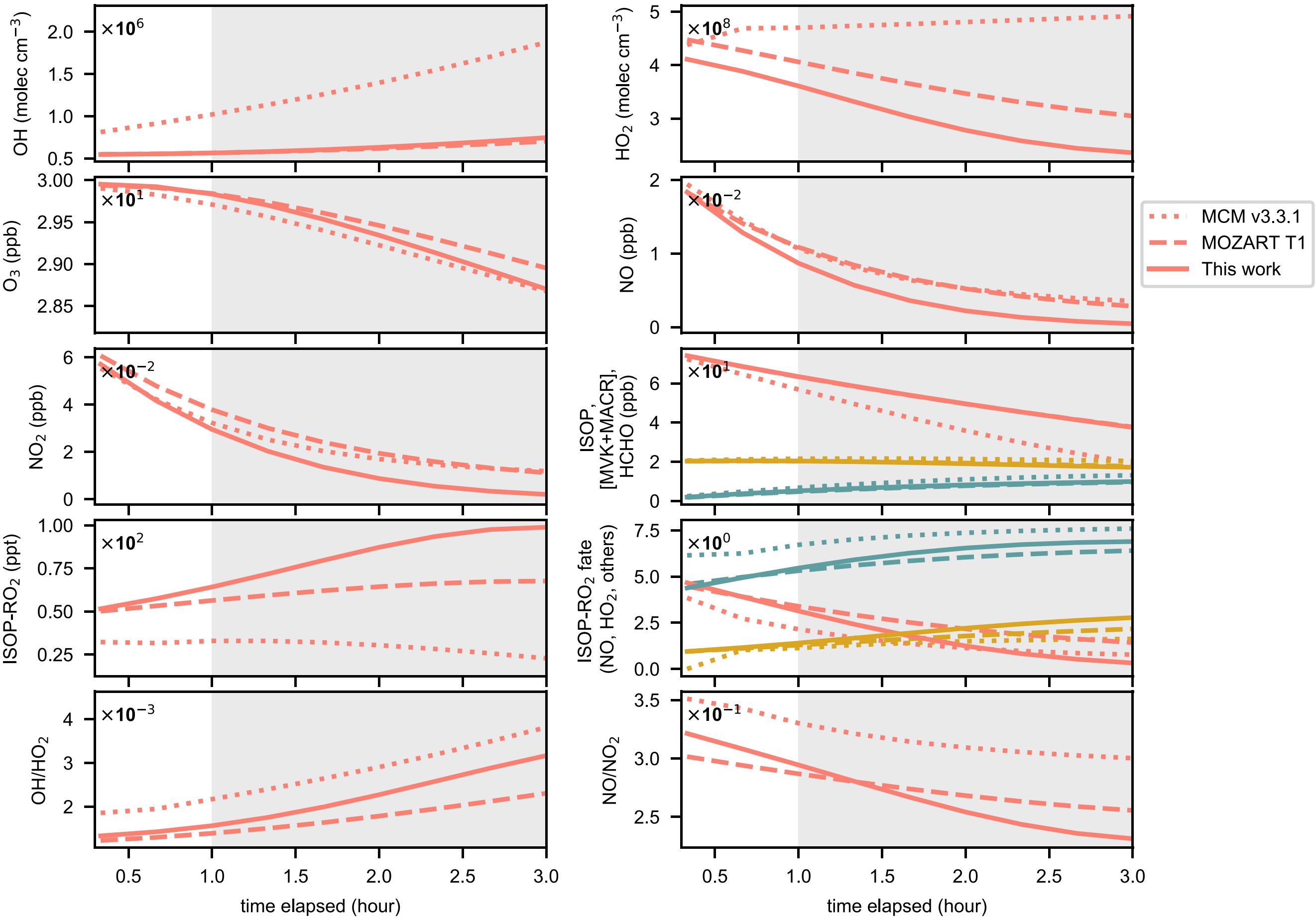

Figure 3. Chemical evolution from box-model simulations of the different chemical mechanisms as a function of time since the simulation start for clean conditions. For plots with multiple quantities, the first quantity listed on the *y*-axis label is orange, the second is teal, and the third is gold. The first hour is dictated by initial conditions and a few reactions and does not represent the full behavior of the mechanisms so we focus on the final 2 hr, highlighted in gray.

from Nature (MEGAN) framework (e.g., Guenther et al., 2006, 2012). Simulated isoprene emission (E_{isop}) at each layer follows:

$$E_{\mathrm{isop}} = \mathrm{LAD}\, \varepsilon_i\, \gamma_{T_l}\, \gamma_{\mathrm{PPFD}} \tag{2}$$

The emission capacity (ε_{i}) is a constant equal to 10,000 μg m^{-2} hr^{-1} for isoprene emission from broadleaf deciduous temperate trees (Guenther et al., 2012). However, we use ε_i equal to 3,000 μg m^{-2} hr^{-1} to obtain reasonable mean in-canopy mixing ratios of isoprene (i.e., less than 10 ppbv). As stated by Guenther et al. (2012), there often needs to be a model specific tuning parameter to get reasonable emissions from MEGAN for a particular model (i.e., the canopy environment coefficient), and we interpret our reduction in ε_{i} as resulting from that need. The activity factors (γ) for leaf temperature (T_{l}) and leaf-level photosynthetic photon flux density (PPFD) are calculated separately for sunlit versus shaded leaves and then averaged using the fraction of sunlit leaves at each layer.

The T_{l} activity factor (γ_{T_l}) follows:

$$\gamma_{T_l} = E_{\mathrm{opt}} \frac{C_{T_2}\, e^{\frac{C_{T_1}}{R}\left(\frac{1}{T_{\mathrm{opt}}}-\frac{1}{T_l}\right)}}{C_{T_2} - C_{T_1}\left(1 - e^{\frac{C_{T_2}}{R}\left(\frac{1}{T_{\mathrm{opt}}}-\frac{1}{T_l}\right)}\right)} \tag{3}$$

Parameters C_{T_1} (95 kJ mol^{-1}) and C_{T_2} (230 kJ mol^{-1}) are the activation and deactivation energies; R is the ideal gas constant (kJ K^{-1} mol^{-1}); T_l is in units K; E_opt (1.9; unitless) is the maximum normalized emission capacity; T_opt (312.5 K) is the T_l at which E_opt occurs. Values for E_opt and T_opt follow Guenther et al. (1999).

The PPFD activity factor (γ_P) follows:

$$\gamma_\text{P} = C_\text{P}\frac{\alpha\text{PPFD}}{\sqrt{1+\alpha^2\text{PPFD}^2}} \tag{4}$$

The variable PPFD is in μmol m^{-2} s^{-1}; C_P (unitless) and α (mol mol^{-1}) follow Guenther et al. (2006):

$$\alpha = 0.004 - 0.0005\ln\left(\text{PPFD}_{240}\right) \tag{5}$$

$$C_\text{P} = 0.0468\,\text{PPFD}_{240}{}^{0.6}\,e^{0.005\left(\text{PPFD}_{24}-\text{PPFD}_0\right)} \tag{6}$$

The variable C_P is the normalized emission capacity at PPFD = 1000 μmol m^{-2} s^{-1} and α is the quantum yield of isoprene. The variable PPFD_{240} is the average PPFD over the past 240 hr and PPFD_{24} is the average PPFD over the past 24 hr. We halve the instantaneous PPFD to estimate PPFD_{240} and PPFD_{24}—given that we stimulate mid-day conditions, halving instantaneous values should approximate daily averages. The constant PPFD_0 is equal to 200 μmol m^{-2} s^{-1} for sunlit leaves and 50 μmol m^{-2} s^{-1} for shaded leaves (Guenther et al., 2006).

2.3.2. Soil

Only NO is emitted by the soil in our model. We perform two NCAR-LES-MLM-CHEM simulations: the first case is a lower bound and the second is an upper bound of observed soil NO emissions for temperate deciduous forests. The micrometeorology of the two cases can be considered the same (Table 1). The case high_soil_NO has 15 pptv m s^{-1} soil NO emissions and low_soil_NO has 3 pptv m s^{-1}. The slim constraints on chamber soil NO fluxes from deciduous forests in the southeast US range from 0.1 to 15 pptv m s^{-1} (Thornton et al., 1997; Valente & Thornton, 1993; Williams & Fehsenfeld, 1991).

We note that NO emitted by the soil faces parameterized transport from the soil surface to 1 m (the lowest grid cell of the LES). Because we did not modify MOST to account for chemical reactivity, no chemistry occurs from 0 to 1 m. Therefore, the mean soil NO source to the model should be regarded as the mean NO_x flux at 1 m (14.0 pptv m s^{-1} in high_soil_NO and 2.6 pptv m s^{-1} in low_soil_NO). We do not tie our soil NO emission to soil moisture and temperature given that they do not change much on the timescales investigated here.

2.4. Dry Deposition

2.4.1. Description of Framework and Processes in Multilayer Dry Deposition Scheme

Dry deposition is parameterized at each vertical layer of the canopy using a resistance framework, with dry deposition for different gases varying with their molecular weight, reactivity, and solubility, as is common in dry deposition schemes (e.g., Wesely, 1989; Wesely & Hicks, 2000; Zhang et al., 2002). Other than in this broad sense, however, our scheme differs from widely used approaches (we discuss the differences in Section 2.4.2). Below we outline exactly how we calculate dry deposition. In our model, all reactants deposit to leaves and soil. Note that the parameterization for dry deposition described here differs from that described by Clifton and Patton (2021) for ozone because here we need to simulate dry deposition of many species within the same framework.

Leaf deposition terms are calculated separately at each canopy layer for sunlit versus shaded leaves, and then averaged according to the local sunlit versus shaded leaf fraction. Resulting from the need for parallel stomatal and cuticular uptake pathways on the lower side of the leaves but only cuticular uptake on the upper side (see next paragraph), leaf uptake at each height in the canopy ("effective leaf conductance" or eg_leaf [s^{-1}]) follows:

$$eg_\text{leaf} = eg_\text{leaf,up} + eg_\text{leaf,lo} \tag{7}$$

The subscripts "up" and "lo" refer to the upper and lower sides of leaves.

$$eg_\text{leaf,up} = \left[\frac{1}{g_\text{b}} + \frac{1}{g_\text{leaf,up}}\right]^{-1}\text{LAD} \tag{8}$$

Table 5
The Initial Resistances Used for All Species in the Dry Deposition Scheme

Initial resistances	Value (s m^{-1})
$R_{\mathrm{i,s,cut}}$	1×10^{8}
$R_{\mathrm{i,r,cut}}$	1×10^{3}
$R_{\mathrm{i,s,m}}$	5×10^{5}
$R_{\mathrm{i,r,m}}$	5×10^{0}
$R_{\mathrm{i,s,soil}}$	1×10^{8}
$R_{\mathrm{i,r,soil,wet}}$	1×10^{4}
$R_{\mathrm{i,r,soil,dry}}$	1×10^{2}

$$e g_{\mathrm{leaf,lo}} = \left[\frac{1}{g_{\mathrm{b}}} + \frac{1}{g_{\mathrm{leaf,lo}}}\right]^{-1} \mathrm{LAD} \tag{9}$$

The variable g_{b} (m s^{-1}) is the conductance for transport of a gas through the leaf boundary layer, and g_{leaf} (m s^{-1}) is the conductance for removal of a gas on the upper or lower side of the leaf.

We consider that the trees only have stomata on one side of their leaves, consistent with broadleaf deciduous vegetation, but have cuticles on both sides of their leaves. The structure of our dry deposition scheme with regards to the upper and lower sides of the leaves follows Monteith and Unsworth (1990) and Nobel (1991).

The variable g_{b} is calculated with the same model as heat: the maximum of values for free and forced convection (Leuning et al., 1995; Nikolov et al., 1995):

$$g_{\mathrm{b,H,free}} = 0.921 \frac{D_{\mathrm{H}} \left(\kappa\, g \,|\, T_{\mathrm{a}} - T_{\mathrm{l}} \,|\, l_{\mathrm{l}}^{3} / \upsilon^{2}\right)^{0.25}}{l_{\mathrm{l}}} \tag{10}$$

$$g_{\mathrm{b,H,forced}} = 0.003 \sqrt{\frac{\|\boldsymbol{u}\|}{l_{w}}} \tag{11}$$

$$g_{\mathrm{b}} = \left(\frac{D_{X}}{D_{\mathrm{heat}}}\right)^{\frac{2}{3}} \max\left[g_{\mathrm{b,H,free}},\; g_{\mathrm{b,H,forced}}\right] \tag{12}$$

The variable D_X is molecular diffusivity of gas X in air (m^2 s^{-1}); D_{H} is the molecular diffusivity for heat in air (m^2 s^{-1}); κ is a coefficient for the volumetric thermal expansion of air (K^{-1}); g is the acceleration due to gravity (m s^{-2}); T_{a} is air temperature (K); l_{l} is the leaf length (0.15 m); υ is the kinematic viscosity of dry air (m^2 s^{-1}); $\boldsymbol{u}$ is the wind vector (m s^{-1}); l_w is the leaf width (0.05 m).

For upper and lower sides of the leaf, g_{leaf} (m s^{-1}) follows:

$$g_{\mathrm{leaf,up}} = g_{\mathrm{cut}} \tag{13}$$

$$g_{\mathrm{leaf,lo}} = \frac{1}{\left(\frac{1}{g_{\mathrm{s}}} + \frac{1}{g_{\mathrm{m}}}\right)} + g_{\mathrm{cut}} \tag{14}$$

The variable g_{cut} is the cuticular conductance (m s^{-1}), which describes the ability of leaf cuticle to remove the gas via the gas's solubility and reactivity, follows:

$$g_{\mathrm{cut}} = f_{\mathrm{wet,cut}} \left(\frac{H_X^{\mathrm{eff}}\,\mathrm{R\,T}}{R_{\mathrm{i,s,cut}}} + \frac{f_{0,X}}{R_{\mathrm{i},r,\mathrm{cut}}}\right) + \left(1 - f_{\mathrm{wet,cut}}\right)\left(\frac{f_{0,X}}{R_{\mathrm{i},r,\mathrm{cut}}}\right) \tag{15}$$

The variable H_X^{eff} is the effective Henry's Law constant at 298.15 K (M atm^{-1}) for gas X; $\boldsymbol{R}$ is the universal gas constant (atm M^{-1} K^{-1}); $T = 298.15$ K; $f_{0,X}$ is the reactivity of gas X with the surface, which scales from 0 to 1 (unitless). The parameter $\boldsymbol{R}_{\mathrm{i,s,cut}}$ (s m^{-1}) is the initial resistance for solubility on cuticles and $\boldsymbol{R}_{\mathrm{i,r,cut}}$ (s m^{-1}) is the initial resistance for reactivity on cuticles (Table 5).

The variable $f_{\mathrm{wet,cut}}$ is the fraction of wet leaf cuticle (unitless) and estimated via:

$$f_{\mathrm{wet,cut}} = e^{\mathrm{RH_l}} / e \tag{16}$$

e is the natural number (Euler's number); $\mathrm{RH_l}$ is leaf-level fractional relative humidity because thin water films form on leaf cuticles as humidity increases (Burkhardt & Eiden, 1994; Burkhardt & Hunsche, 2013; Eiden et al., 1994). The assumption in Equation 16 is that a greater fraction of the leaf becomes covered by the water film as $\mathrm{RH_l}$ increases. We use an exponential dependence because nonstomatal dry deposition of ozone has been shown to depend on relative humidity exponentially—current understanding is that this dependence is due to thin water film formation on leaf cuticles (Clifton et al., 2020; Sun et al., 2016).

The stomatal conductance (g_s) (m s^{-1}) describes the ability of the gas to diffuse through plant stomata, and follows:

$$g_s = \frac{D_x}{D_{H_2O}} g_{s,H_2O} \tag{17}$$

The parameter D_{H_2O} is the molecular diffusivity of water vapor in air. The variable g_{s,H_2O} is the stomatal conductance for water vapor and follows the Ball-Berry model (Ball et al., 1987):

$$g_{s,H_2O} = \left[g_0 + g_1 \frac{A_{net}}{c_s} p_s \, \mathrm{RH}_l \right] \frac{\mathrm{R\,T}_a}{p_s} \tag{18}$$

The parameters g_0 (0.01 mol m^{-2} s^{-1}) and g_1 (9; unitless) are vegetation type specific and empirical; A_{net} is net photosynthesis (mol m^{-2} s^{-1}); c_s is the carbon dioxide partial pressure at the leaf surface (Pa); p_s is the atmospheric surface pressure (Pa); R is the universal gas constant (J mol^{-1} K^{-1}). An iterative framework for the carbon dioxide partial pressure inside the leaf couples A_{net} to g_s (see Text S1 of Clifton and Patton (2021) for full details).

The mesophyll conductance (g_m) (m s^{-1}) is calculated via:

$$g_m = \frac{H_X^{\mathrm{eff}} \mathrm{R\,T}}{R_{i,s,m}} + \frac{f_{0,X}}{R_{i,r,m}} \tag{19}$$

The variable g_m describes the ability of the fluids and tissues internal to the leaf (e.g., the mesophyll) to remove the gas via the gas's reactivity and solubility. The parameter $R_{i,s,m}$ (s m^{-1}) is the initial resistance for solubility inside the leaf and $R_{i,r,m}$ (s m^{-1}) is the initial resistance for reactivity instead the leaf (Table 5).

The conductance for soil (g_{soil}) (m s^{-1}) follows:

$$g_{soil} = f_{wet,soil} \left(\frac{H_X^{\mathrm{eff}} \mathrm{R\,T}}{R_{i,s,soil}} + \frac{f_{0,X}}{R_{i,r,soil,wet}} \right) + (1 - f_{wet,soil}) \left(\frac{f_{0,X}}{R_{i,r,soil,dry}} \right) \tag{20}$$

The parameter $R_{i,s,soil}$ (s m^{-1}) is the initial resistance for solubility on soil, $R_{i,r,soil,wet}$ (s m^{-1}) is the initial resistance for reactivity on wet soil, and $R_{i,r,soil,dry}$ is the initial resistance for reactivity on dry soil (Table 5). The construction of our model, specifically the use of different initial resistances for f_0 for wet versus dry conditions is based on evidence for ozone that dry deposition to soil decreases with increasing soil moisture (Clifton et al., 2020; Fumagalli et al., 2016; Massman, 2004; Stella et al., 2019). The variable $f_{wet,soil}$ is the fraction of wet soil (unitless) and follows:

$$f_{wet,soil} = \mathrm{vsm}_{0.5m} \tag{21}$$

The variable $\mathrm{vsm}_{0.5m}$ is the volumetric soil moisture at 0.5-m depth in the soil (m^3 m^{-3}).

Parameterized transport through the soil boundary layer is combined with parameterized turbulent transport from 1 m to the soil boundary layer. Thus, we do not adjust transport through the soil boundary layer by the gas's diffusivity.

2.4.2. Comparison of Dry Deposition Scheme to Wesely (1989)

The Wesely (1989) dry deposition scheme (hereinafter, Wesely) is the most widely used and recognized dry deposition scheme and has been a key building block for both big leaf and multilayer canopy parameterization development over the past 30 years. Our dry deposition scheme differs from Wesely so we identify the differences to illustrate that regardless of scale, the processes and dependencies are represented in distinct ways:

1. Our model is an MLM so we estimate leaf uptake at multiple vertical canopy layers (currently 10) in contrast to Wesely who only estimate leaf uptake at two canopy layers.
2. Turbulence is resolved in our model, which eliminates the need for parameterizations of turbulent transport above or inside the canopy except at the ground where our model has a rough-wall boundary condition.

3. Wesely uses a single bulk term to describe transport through the thin boundary layer around all surfaces. In our model, transport through the boundary layer around surfaces differs for soil and leaves (and for leaves is calculated at each canopy layer). As such, our models for boundary layers around surfaces are also different from Wesely.
4. The original big-leaf Wesely scheme employs seasonal parameters instead of leaf area index (LAI; i.e., LAD integrated over the canopy) while our leaf conductances are scaled by LAD.
5. Our model provides an estimate of carbon dioxide exchange across stomata driven by the carbon supply and demand for photosynthesis, rather than a limited Jarvis (1976) type stomatal conductance model where a prescribed maximum stomatal conductance is scaled by meteorological factors as used in Wesely.
6. Wesely assumes dry deposition on a given surface depends on the gas's solubility and reactivity but does not distinguish between wet versus dry surfaces (i.e., a gas's solubility always increases uptake, even if the part of the leaf is not explicitly wet; e.g., Knote et al., 2015; Hardacre et al., 2021). However, the surface needs to be wet for a gas to dry deposit due to its high solubility. While we can assume that after diffusion through stomata, the surfaces inside the leaf are wet, soil and cuticles are not always wet. In our model, a gas's solubility only impacts uptake to wet surfaces while a gas's reactivity impacts dry deposition to wet and dry surfaces.
7. While Wesely includes adjustments to cuticular uptake in the upper canopy due to leaf wetness from rain and dew, the formation of thin water films on leaves (Burkhardt & Eiden, 1994; Burkhardt & Hunsche, 2013; Eiden et al., 1994) is not represented by Wesely. In our model, we include the formation of thin water films on leaves.
8. Leaf wetness does not reduce stomatal uptake in our model, in contrast to Wesely. Leaf wetness also does not reduce cuticular uptake of ozone, as suggested by Wesely for some cases, as is consistent with evidence showing enhancements of cuticular uptake of ozone on wet leaves (Clifton et al., 2020; Massman, 2004; Sun et al., 2016).
9. In our model, cuticular uptake happens on both sides of the leaf, but stomatal uptake happens only on one side, as consistent with broadleaf deciduous vegetation. In Wesely, any distinction as to whether cuticular uptake happens on a single side or both sides is not explicit. Theoretically, cuticular uptake could happen on both sides, but the reactivity of the cuticle and the water films or droplets on the cuticle may differ between the sides (Clifton et al., 2020). Regardless, we assume that cuticular reactivity and thin water film formation are the same on both sides. Without this assumption, we do not capture the highest v_d observed across gases for H_2O_2, HNO_3, and HMHP (see Section 2.4.3).
10. Wesely does not consider changes in soil uptake with soil moisture. We use a similar framework for soil uptake as cuticular uptake and we parameterize the fraction of dry versus wet soil with volumetric soil moisture at 0.05-m depth.

In summary, our dry deposition scheme is fundamentally different from Wesely aside from a general resistance framework incorporating molecular weight, solubility, and reactivity influences on uptake. While the exact Wesely scheme determines uptake at two layers in a canopy, our scheme can estimate uptake for several layers in a canopy providing a detailed vertical distribution of dry deposition with key differences in the representation of individual processes.

2.4.3. Tuning Strategy for Initial Resistances

The initial resistances in our dry deposition scheme are the same across all gases and need to be tuned. Without a comprehensive flux data set for all the gases in our chemical mechanism, or even constraints on the fluxes of many of them, we turned to one of the most comprehensive reactive flux datasets for a deciduous forest to define the initial resistances: the Nguyen et al. (2015) data set from 5 days in June 2013 at Centerville, Alabama. Nguyen et al. (2015) report fluxes for hydrogen cyanide (HCN), hydrogen peroxide (H_2O_2), formic acid, nitric acid (HNO_3), hydroxymethyl hydroperoxide (HMHP), hydroxyacetone (HAC), peroxyacetic acid (PAA), the C_4 hydroxy dicarbonyl from IEPOX oxidation (HDC4), the C_4 dihydroxy carbonyl from IEPOX oxidation (DHC4), isoprene hydroperoxy aldehydes (HPALD), the sum of isoprene hydroxy hydroperoxides and epoxydiols ([ISOPOOH + IEPOX]), propanone nitrate or propanal nitrate (PROPNN), isoprene hydroxy nitrates (ISOPN), the sum of hydroxy nitrates with carbon backbones of methacrolein and methyl-vinyl ketone ([MACN + MVKN]), isoprene nitrooxy hydroperoxide (INP), and monoterpene nitrooxy hydroperoxide (MTNP).

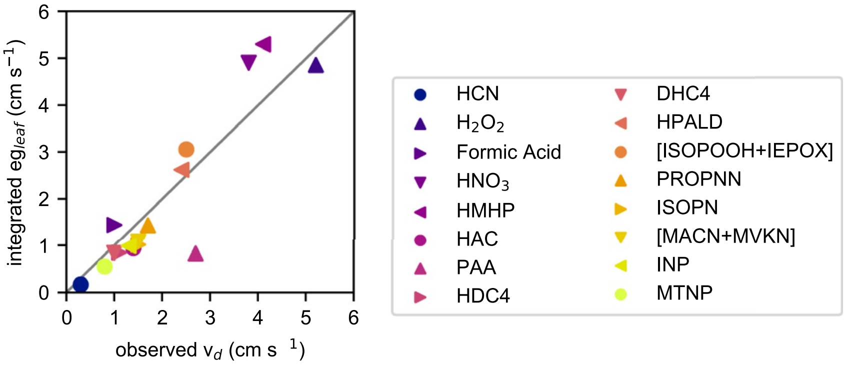

Figure 4. Observed deposition velocity (v_d) at Centerville, Alabama versus effective leaf conductance (eg_{leaf}) integrated through the canopy as estimated with our multilayer dry deposition scheme. Daytime average v_d are from Nguyen et al. (2015) Table S2.

Specifically, we estimated eg_{leaf} with our dry deposition scheme for the species in the Nguyen et al. (2015) data set. We tuned the initial resistances needed for our model by comparing eg_{leaf} integrated through the canopy (hereinafter, integrated eg_{leaf}) calculated with our scheme to observed v_d from Nguyen et al. (2015) (see their Table S2 for exact values used). In general, observed v_d include the influences of not only leaf uptake (i.e., eg_{leaf}) but also turbulent transport, fast chemical losses, dry deposition to soil, and changes due to nonstationarity. However, Nguyen et al. (2015) suggest that the observed ranking of v_d across the gases in their data set from high to low values is dominated by leaf uptake, justifying our comparison of integrated eg_{leaf} with the observed v_d as the basis of our tuning.

We estimate eg_{leaf} for the gases from Nguyen et al. (2015) using simple Henry's Law constants, diffusivities, and reactivities as defined in Nguyen et al. (2015)'s Table S2 as well as archived vertical profiles of meteorological and biophysical variables from an existing simulation with the NCAR-LES-MLM (Clifton & Patton, 2021) that has similar midday conditions as observed at Centerville during the period of measurements. For example, potential temperature at canopy top is 30.5°C in our simulation within the range of the observed midday virtual temperature around 28-35°C, relative humidity is 61%–62% in our simulation within the range of observed daytime relative humidity of 50%–80%, and friction velocity at canopy top is 0.39 m s^{-1} in our simulation and about 0.36–0.46 m s^{-1} observed midday. Sensible heat flux at canopy top in our simulation is 133 W m^{-2} compared to an observed 140–160 W m^{-2} midday and latent heat flux is 422 W m^{-2} compared to an observed 450 W m^{-2} midday. Our simulation is for a 20-m high homogeneous broadleaf deciduous forest with LAI of 4 m^2 m^{-2}, which differs from Talladega National Forest that surrounds the Centerville site on three sides with an LAI of 4.7 m^2 m^{-2} and 10-m canopy height. However, similar micrometeorology suggests that LAI and canopy height differences should not preclude development of an empirical dry deposition scheme appropriate for use here.

Figure 4 shows good agreement between the observed v_d and the integrated eg_{leaf} using the initial resistances in Table 5. Our tuning is primarily guided by the range in solubilities across the gases in the observational data set. The parameters related to solubility and leaf uptake are $R_{i,s,cut}$ and $R_{i,s,meso}$. The Nguyen et al. (2015) data set has only four gases with non-zero f_0: H_2O_2 and HNO_3 ($f_0 = 1$) as well as PAA and HMHP ($f_0 = 0.1$). H_2O_2, HNO_3 and HMHP are also highly soluble. Thus, it is challenging to tune based on reactivity relative to solubilities and molecular weights, for which there are more even distributions of different values across the gases. Our offline estimate slightly overestimates dry deposition of HNO_3 and HMHP but underestimates dry deposition of H_2O_2 (slightly) and PAA (majorly) (Figure 4), suggesting that the reactivity influence is underestimated, and the solubility influence is overestimated across these gases. However, increasing the influence of reactivity would lead to less-than-ideal ozone dry deposition and we thus do not tune the initial resistances further. For example, ozone has $f_0 = 1$ and very low solubility. With our offline dry deposition scheme employing the parameters values in Table 5, integrated eg_{leaf} for ozone is 1.4 cm s^{-1} with 58% stomatal uptake. Ozone fluxes were not measured by Nguyen et al. (2015) but observed midday v_d for ozone span ~0.2–1.4 cm s^{-1} at mid-latitude forested monitoring sites (Bauer et al., 2000; Clifton et al., 2017, 2019; Finkelstein et al., 2000; Mikkelsen et al., 2004; Neirynck & Verstraeten, 2018; Turnipseed et al., 2009; Wu et al., 2018), suggesting integrated eg_{leaf} falls on the higher end of observations. The daytime stomatal fraction of ozone dry deposition inferred from observations at forested sites averages 57% (Clifton et al., 2020), and so we capture the stomatal fraction. Because stomatal uptake of ozone is already the highest possible value for a given g_s (i.e., there no mesophyll resistance for ozone), increasing the influence of the reactivity would increase cuticular uptake of ozone, decreasing the stomatal fraction and most importantly increasing eg_{leaf} to unrealistic values, which we wish to avoid.

For the reactants in the chemical mechanism in the NCAR-LES-MLM-CHEM, we use f_0 from the Community Earth System Model (CESM; Emmons et al., 2020; Karl et al., 2010; Schwantes et al., 2020). Table 2 gives f_0 for each reactant. For CO, NO, methane, and isoprene, $f_0 = 0$. For HO_2, NO_2, and N_2O_5, $f_0 = 0.1$. For other reactants, $f_0 = 1$. Note that while we do not use $f_0 = 0$ for HPALD and [ISOPOOH + IEPOX]) as suggested by Nguyen et al. (2015) and used in our offline tuning, employing $f_0 = 1$ for these reactants does not change leaf uptake, which is mostly dominated by cuticular uptake due to the moderate-to-high solubilities as well as the high molecular weights that slow diffusion through stomata.

NO_2 reacts inside stomata, but there is not much evidence suggesting cuticular uptake of NO_2 (Chaparro-Suarez et al., 2011; Delaria et al., 2020; Sparks et al., 2001). With $f_0 = 0.1$, the stomatal fraction of leaf uptake for NO_2 is 93%. To our knowledge, only Delaria et al. (2020) infers mesophyll resistances for NO_2—their values are 20–130 s m^{-1} for Californian trees. Our choice of $R_{\mathrm{i,r,meso}}$ allows the mesophyll resistance for NO_2 to fall within this range and stomatal uptake of ozone to be unobstructed by the mesophyll, as supported by laboratory evidence (Laisk et al., 1989; Omasa et al., 2000; Wang et al., 1995).

To parameterize dry deposition to the soil, we started with the same initial resistances for soil uptake as cuticular uptake in our tuning but increased the initial resistance for reactivity on wet soil by a factor of 10, reducing the uptake by surface reaction to wet soil. To get a reasonably high g_{soil} for ozone (i.e., 1 cm s^{-1} for completely dry soil moisture), we reduced the initial resistance for reactivity on dry surfaces by 10. Our parameterization works so that dry deposition of ozone to soil decreases with soil moisture as reactions on dry soil surfaces outweigh reactions on wet soil surfaces (Clifton et al., 2020).

In the NCAR-LES-MLM-CHEM, we use the effective Henry's Law constant like Wesely to indicate the gas's solubility, in contrast to Nguyen et al. (2015) who suggest using the simple Henry's Law constant. In our effective Henry's Law constants, we consider hydrolysis, but not dissociation of acids and bases. Except for H_2O_2, a weak acid, the gases in our mechanism should not have strong protonation tendencies and thus our effective Henry's Law constants can likely adequately describe the solubility.

In general, there is a need for further research into the reactivities (e.g., Niinemets et al., 2014) used in classic approaches for modeling dry deposition (e.g., Wesely, 1989; Zhang et al., 2002). The reactivity term in Wesely is based on “the negative log of electron activity for half redox reactions in neutral aqueous solutions and the overall second order reaction rates with S(IV)” “in water with near neutral pH” “for the oxidation of biological substances” (Wesely, 1989). Wesely likely used the reactivity for aqueous reactions because there were more constraints on aqueous reactions at the time and/or the reactivity term was largely designed for inside plant stomata (e.g., mesophyll) where reactions are aqueous. Thus, there are at least three topics that should be addressed in future work. First, whether the basis for the reactivity term of aqueous reactions is appropriate for both wet and dry surfaces should be evaluated. Second, applying the same reactivity to wet versus dry mesophyll, cuticles, and soil may be inappropriate, given that the composition of these surfaces may vary. Third, using redox reactions to define the reactivity does not make sense for many compounds, including the oxidized biogenic compounds examined here, so a critical re-examination of the definition of the reactivity is needed.

2.5. Chemical Segregation

We consider chemical segregation in the following framework, with the mean chemical sink of X_1 by reaction with X_2 and reaction rate coefficient k at a given height following:

$$\left.\frac{\partial \overline{X_1}}{\partial t}\right|_{\mathrm{chem}} = -\overline{k}\,\overline{X_1 X_2} = -\overline{k}\left(\overline{X_1}\,\overline{X_2} + \overline{X_1' X_2'}\right) = -\overline{k}\,\overline{X_1}\,\overline{X_2}\,(1 + I_s) \tag{22}$$

The overbars represent horizontal averages, and the primes represent deviations from the horizontal average. The covariance between X_1 and X_2 ($\overline{X_1' X_2'}$) reflects similar or dissimilar variability in X_1 and X_2 due to organization in the turbulence transporting X_1 and X_2 and the spatially varying sources and/or sinks of X_1 and X_2.

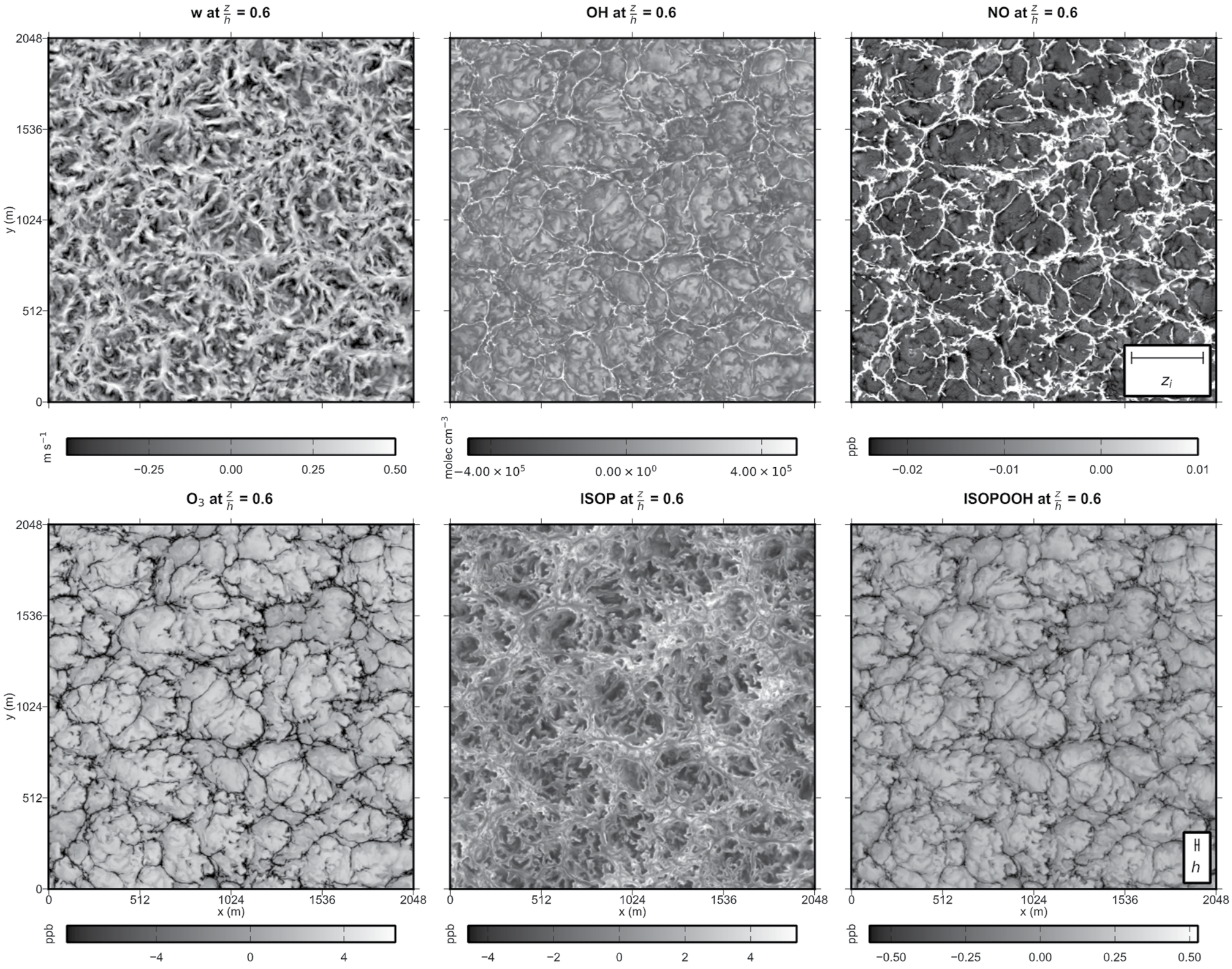

Figure 5. Instantaneous horizontal slices of vertical velocity (w), OH, NO, ozone, isoprene, and ISOPOOH at 0.6 x canopy height (h) for high_soil_NO. Values shown are anomalies from the instantaneous horizontal average. Insets show scale for h and atmospheric boundary layer height (z_i) at the time of the slice.

The segregation intensity (I_s) reflects the magnitude of the covariance relative to $\overline{X_1}\,\overline{X_2}$. Models that assume well-mixed conditions implicitly assume negligible $\overline{X_1'X_2'}$ and thus negligible I_s. Positive I_s means that models assuming complete mixing of reactants underestimate reaction rates while negative I_s implies an overestimate.

Note that the mean and fluctuating components of k could be considered in the framework of segregation and the NCAR-LES-MLM-CHEM considers varying k. However, we expect k fluctuations to be small relative to reactant fluctuations, and therefore do not examine k within the framework of segregation, as done by prior studies (e.g., Kim et al., 2016; Krol et al., 2000). Also note that Equation 22 ignores any sub-grid covariance between X_1 and X_2 because we do not have an appropriate model for this.

3. Spatial Distribution of Reactants Simulated by the NCAR-LES-MLM-CHEM

3.1. Instantaneous Horizontal Variability

Figure 5 shows instantaneous horizontal variability in OH, NO, ozone, isoprene, and ISOPOOH as well as vertical velocity (w) at the height of maximum canopy density in high_soil_NO (i.e., a single instance in time in our midday simulation). Features range in size from canopy height (h) to the ABL height (z_i) for w and all reactants.

For w, upward-moving motions occur in thin-filament-like structures and downward-moving motions occur in broad regions of negative w.

Ozone and ISOPOOH are depleted in the thin upwelling motions, but OH and NO are enriched in them because the canopy is an ISOPOOH and ozone sink but NO source and NO + HO_2 is an important OH source (Figure S2 in Supporting Information S1). Horizontal variability in isoprene is particularly distinct compared to the other reactants, closely following horizontal variability in leaf temperature (not shown). Above the canopy at $2h$, the structure of the horizontal variability is much larger for w and all reactants (Figure S3 in Supporting Information S1). The small-scale variations observed at $0.6h$ (Figure 5) and even more exaggeratedly so at the ground (Figure S4 in Supporting Information S1) are not as clearly present at $2h$, highlighting the impact of the canopy on turbulence.

In low_soil_NO, some features of OH and NO horizontal variability change relative to high_soil_NO (compare Figure S5 in Supporting Information S1 with the upper right two panels of Figure 5). For example, the filament-like upwelling motions with enriched NO are slightly thinner in low_soil_NO at $0.6h$. Additionally, horizontal variability in OH at $0.6h$ tends to have larger structure in low_soil_NO (like the horizontal variability in ISOPOOH and ozone in high_soil_NO in Figure 5). In contrast to high_soil_NO, OH is not enriched in the thin upwelling motions which contain high NO, rather OH is depleted in low_soil_NO. The difference between cases likely results from enhanced secondary OH production in high_soil_NO (Figure S2 in Supporting Information S1).

3.2. Mean Vertical Profiles

Figure 6 shows the vertical profiles of the mean abundances for the reactants in the chemical mechanism. The effect of the canopy is apparent in most of the profiles. Most profiles are relatively constant above h, except isoprene, which decreases above h. The reactants with canopy-bottom minima in their profiles are HO_2, O_3, H_2O_2, N_2O_5, and the reactive carbon oxidation products (CH_3O_2, HCHO, $ISOPAO_2$, $ISOPBO_2$, ISOPOOH, XO_2, [HYDRALD + HPALD], and [MVK + MACR]). The oxidation products maximize above h. We expect the maxima in the oxidation products to occur above h because the canopy is an efficient sink of these compounds through dry deposition. Isoprene's maximum happens at $0.8h$, where isoprene emissions maximize (not shown), which is slightly above maximum LAD at $0.6h$ but where the sunlight fraction of leaves exceeds the shaded fraction of leaves (Figure 1). Horizontal mean isoprene is maximum 9.7 ppbv, which is on the higher side of daytime hourly isoprene mixing ratios observed at temperate deciduous forests (Goldstein et al., 1998; Helmig et al., 1998; McKinney et al., 2011; Wei et al., 2020). Both NO and NO_2 peak at the ground, but NO_3 and N_2O_5 peak just above the ground in the lower canopy. Elevated NO_3 below canopy relative to above canopy was also observed at a mixed forest and was attributed to lower below-canopy NO_3 photolysis (Schulze et al., 2017).

Differences with soil NO emissions are also apparent for many reactants. In high_soil_NO relative to low_soil_NO, the abundances of NO, NO_2, NO_3, N_2O_5, OH, and HO_2 are higher but CH_3O_2, $ISOPAO_2$, $ISOPBO_2$, and XO_2 are lower. Other species have similar abundances between cases. Differences between the cases in N_2O_5, HO_2, CH_3O_2, $ISOPAO_2$, $ISOPBO_2$, and XO_2 are largely consistent with height, whereas for OH, NO, NO_2, and NO_3 differences are strongest in the canopy. In high_soil_NO, OH strongly peaks at the ground, and there is a strong decrease in OH upwards from the ground to a local minimum mid-canopy. In low_soil_NO, OH weakly peaks above h and is relatively constant in the lower canopy. In both cases, OH increases with height within the canopy above $0.6h$ but becomes constant above h. High OH near the ground in high_soil_NO follows high local secondary OH production (Figure S2 in Supporting Information S1).

The horizontal mean NO/NO_2 ratio is constant above h around 0.36–0.41 in both cases but varies substantially within the canopy (Figure S6 in Supporting Information S1), another line of evidence that the chemistry is very different at different heights of the canopy. In low_soil_NO, the ratio varies from 0.23 to 0.77 inside the canopy. In high_soil_NO, the ratio varies from 0.33 to 1.37 inside the canopy. Thus, with higher soil NO, more NO_x is NO inside the canopy. In both cases, the ratio peaks at ground due to NO emission at the soil surface and decreases from the ground to the lower canopy with increasing NO + O_3 forming NO_2 and little NO_2 photolysis in the shaded canopy. The ratio then increases from the lower to upper canopy with increasing NO_2 photolysis and less shading.

Horizontal variability in the reactants also varies with height in the canopy. For reactants other than CO and methane, which do not vary much relative to the magnitude of their mixing ratios, horizontal variability in reactant

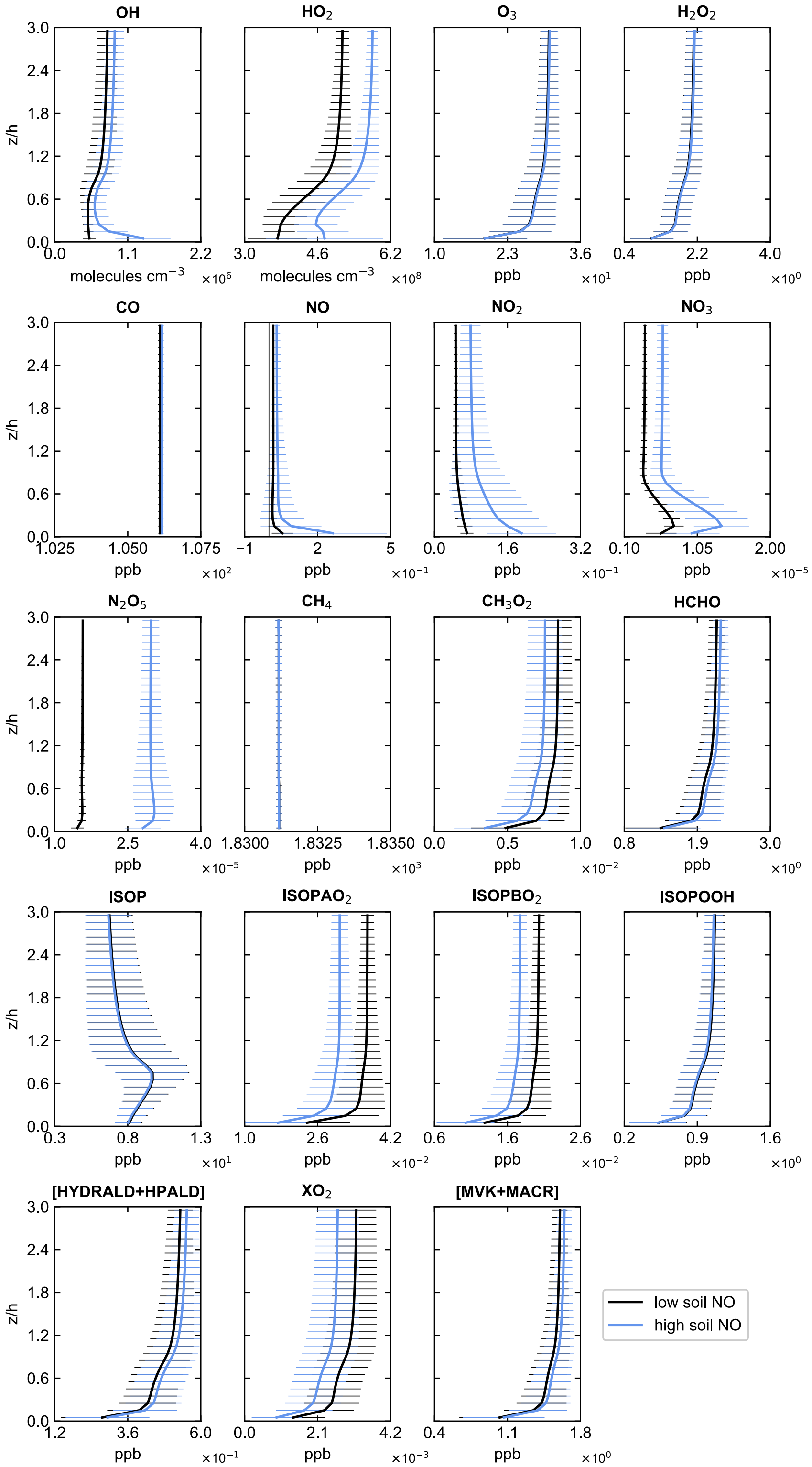

Figure 6. Vertical profiles of the horizontal mean mixing ratios for the reactants in the chemical mechanism (concentrations for OH and HO_2) from the ground to 3 x canopy height (h). Error bars indicate one standard deviation (horizontal variability). Thin gray line on NO panel denotes $x = 0$.

abundances is largest inside the canopy (Figure 6 and Figure S7 in Supporting Information S1). For isoprene, horizontal variability is largest at *h*. There is also a peak in the coefficient of variation (standard deviation divided by mean at same height) for OH at *h* in both cases (with a primary peak at the ground in high_soil_NO). Otherwise, reactants mostly have horizontal variability maxima near or at the ground. NO has the strongest horizontal variability, with the peak in its variability in the lower canopy (coefficient of variation is up to 173% in high_soil_NO and up to 113% in low_soil_NO). NO_2 also has large horizontal variability compared to other gases in high_soil_NO—the coefficient of variation for NO_2 is up to 70% (in contrast with up to 28% in low_soil_NO).

NO variability is also highly skewed, causing the standard deviation error bars on the horizontal mean NO mixing ratio in high_soil_NO to span zero on Figure 6 (note that NO never attains negative values in the simulations). Edburg et al. (2012) also find high skewness for a passive scalar emitted by the ground, compared to passive scalars emitted by or deposited to the canopy. Like Edburg et al. (2012), we find that NO skewness maximizes at canopy top (not shown). Maximal skewness near canopy top likely results from shear-driven motions generated near *h* intermittently penetrating the canopy and transporting NO upwards (Edburg et al., 2012).

4. Vertical Reactant Flux Profiles Simulated by the NCAR-LES-MLM-CHEM

4.1. Total Fluxes

Figure 7 shows profiles of the vertical total fluxes for all reactants in the mechanism. A vertical reactant flux profile reflects the net vertical transport of the reactant by turbulence; this transport can be altered by chemistry depending on the rate at which chemistry produces or destroys the reactant compared to the rate at which turbulent transport occurs. The total fluxes are the sum of the resolved and sub-grid scale (SGS) fluxes. The sign of the fluxes at *h* indicates whether the canopy layer acts as a net source or sink of the reactant. The canopy layer is a net sink of reactive carbon oxidation products and ozone but net source of isoprene, NO, and NO_2.

Below *h*, there are variations in the fluxes of many species with height. Above *h*, most flux profiles change linearly with height, as expected for reactants with lifetimes longer than the time it takes for turbulence to mix the ABL. For example, methane and CO are very well mixed, and the positive vertical fluxes simply reflect entrainment of air with lower methane and CO abundances from the FT into the ABL. Interestingly, OH, which has a very short lifetime compared to the turbulence mixing time, exhibits nearly linear flux profiles with height above *h*. The linear OH flux profile above the canopy suggests that local OH production compensates for the inability for turbulence to transport OH before it reacts. For $ISOPAO_2$ and $ISOPBO_2$, the fluxes are negative within the canopy and increasingly become closer to zero with increasing height, with the maximum negative flux at the ground. We expect that fast chemistry between $ISOPAO_2$ or $ISOPBO_2$ and NO and/or HO_2 contributes to the high downward fluxes at the ground. The CH_3O_2 and XO_2 fluxes are negative from the ground to 3*h*. The CH_3O_2 and XO_2 flux profiles linearly increase with height, indicating that fast losses are even greater above *h* than below.

Comparing the soil NO cases, the fluxes are substantially different for NO, NO_2, NO_3, N_2O_5, CH_3O_2, $ISOPAO_2$, and $ISOPBO_2$, but only slightly different for OH, HO_2, CO, and XO_2. However, for OH and CO, as well as NO_3 and N_2O_5, there are differences between cases in the sign of the flux, at least at some heights.

The only study reporting HCHO eddy covariance fluxes at a forest show positive daytime fluxes (24 pptv m s^{-1} at noon at a coniferous forest in Colorado during August 2010; DiGangi et al., 2011). Simulated HCHO fluxes are negative, contrasting with the positive observed fluxes. Negative HCHO fluxes follow large sinks at soil and leaf surfaces in our model due to the high solubility and reactivity of HCHO. While there is laboratory and field evidence for HCHO depositional sinks (Filella et al., 2006; Gray et al., 2014; Kramshøg et al., 2018; Li, Su, et al., 2016; Seco et al., 2008; Trowbridge et al., 2020), there is also field evidence for leaf and soil HCHO emissions (DiGangi et al., 2011; Trowbridge et al., 2020). While the presence of large HCHO sinks at canopy and soil surfaces in our model may be justifiable, the sinks as parameterized may overestimate loss because we do not account for desorption (Li, Su, et al., 2016). Too high HCHO dry deposition in our model may contribute to too low HCHO mixing ratios in the canopy. For example, observed afternoon HCHO at a mixed forest in upper Michigan during 8 days in August 2008 are maximum 4.2 ppb above *h* in the afternoon (Galloway et al., 2012). While observed HCHO mixing ratios are as low as 2 ppb during the afternoon (comparable to our simulated mixing ratios), the higher observed levels of HCHO mostly correspond to the higher isoprene levels simulated by our model. Better understanding of HCHO sources and sinks in the canopy will advance our ability to accurately represent HCHO in chemistry MLMs (e.g., Wei et al., 2021; Wolfe et al., 2011).

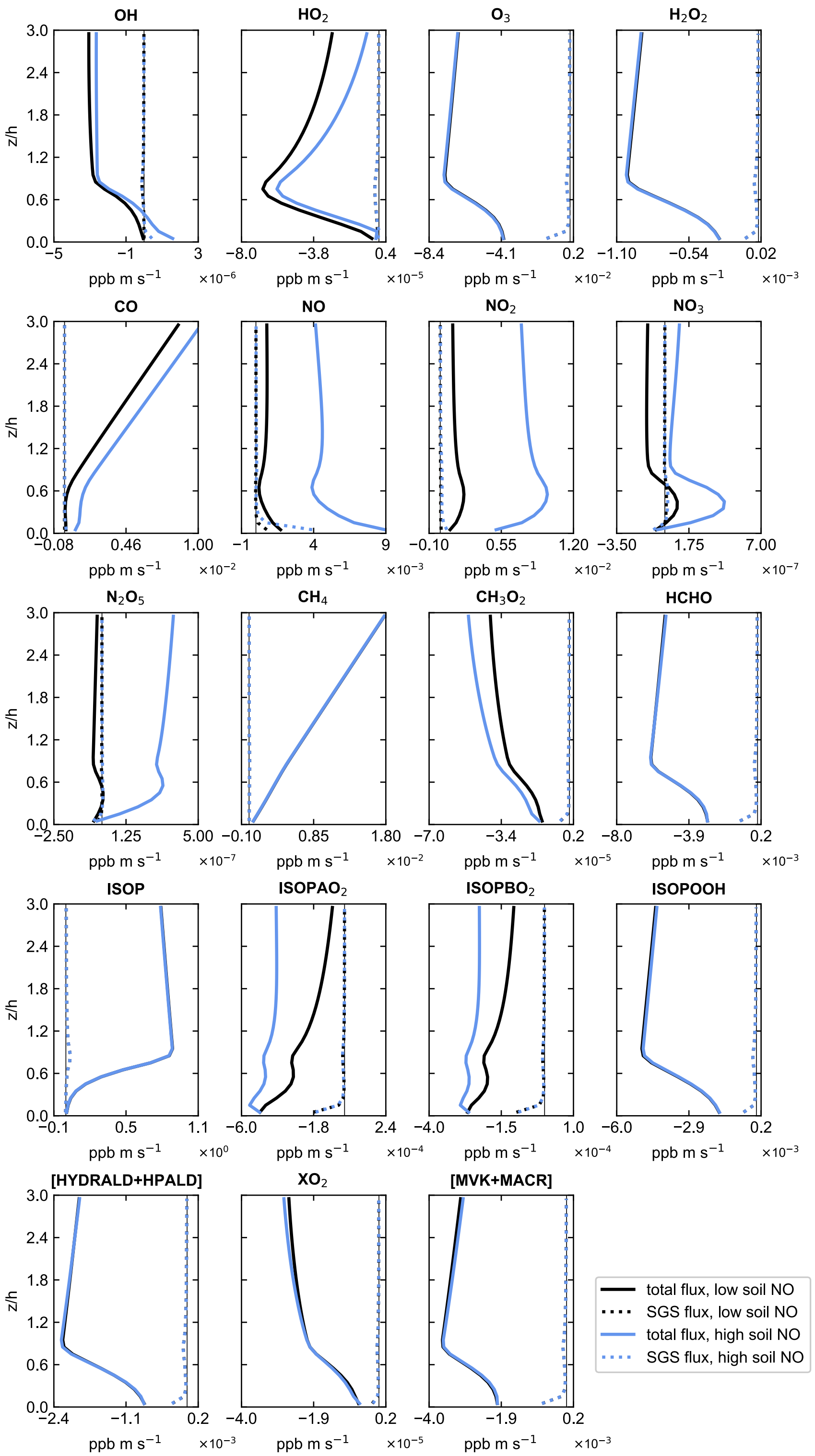

Figure 7. Vertical profiles of the vertical total and sub-grid scale fluxes for the reactants in the chemical mechanism from the ground to 3 *x* canopy height (*h*). Thin gray lines denote *x* = 0.

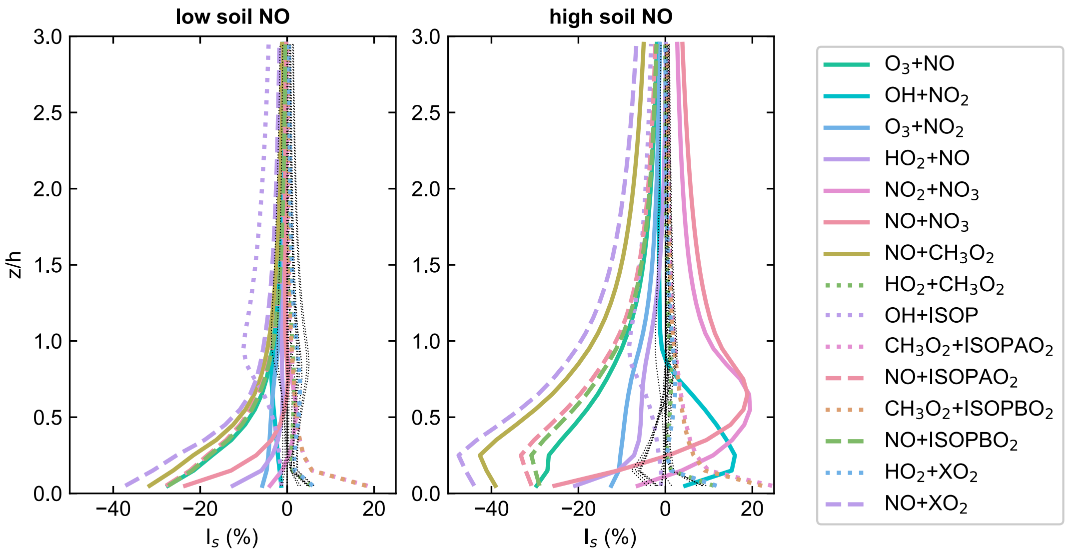

Figure 8. Vertical profiles of the intensities of segregation (I_s) for all the reactions in the chemical mechanism from the ground to 3 x canopy height (h). Dotted lines denote reactions that do not contain NO or NO_2. Color lines denote reactions with substantial segregation intensities in either of the cases (absolute value >10% at least one height within the ground to 3h) or OH + ISOP which we discuss in the text. Other reactions are shown in thin black lines.

4.2. Sub-Grid Scale Flux Contributions

A parameterization in the NCAR-LES-MLM-CHEM is needed to estimate SGS vertical transport. Generally, the impact of the SGS flux on the total flux is minor except at the ground (Figure 7). At the ground, the NO SGS flux is 45% of the total flux. For other gases with non-zero total fluxes at the ground except NO_3 and N_2O_5, the SGS fluxes are less than 40% of the total fluxes at the ground. For NO_3 and N_2O_5, near-surface SGS fluxes are up to 185% of the total fluxes in high_soil_NO, suggesting that NO_3 and N_2O_5 transport there is poorly estimated. Nonetheless, the total NO_3 and N_2O_5 fluxes at the ground are relatively small compared to elsewhere, and the flux divergences are small compared to net chemistry so the poor estimation likely does not matter.

5. Chemical Segregation Inside and Just Above the Forest Canopy Simulated by the NCAR-LES-MLM-CHEM

5.1. Changes With Height and High Versus Low Soil NO Emissions

Figure 8 shows I_s for all the reactions in our mechanism. At least some degree of segregation (i.e., $|I_S| > 1\%$ at some point from 0 to 3h in one of the cases) occurs in each reaction except OH + CO and OH + CH_4. Across all reactions, the highest I_s from 0 to 3h occur within the canopy. In high_soil_NO, I_s range from −19% to +13% across reactions above h but from −48% to +23% below. In low_soil_NO, I_s range from −10% to +4% above h but from −38% to +19% below. Comparing low_soil_NO to high_soil_NO, fewer reactions have substantial in-canopy I_s. In low_soil_NO, large I_s primarily occur in the lower canopy, whereas in high_soil_NO, large I_s occurs in both the lower and upper canopy.

Many reactions have some degree of segregation at the ground, whether positive or negative. Strong segregation at the ground is likely due to shear-driven organized motions generated near the top of the canopy intermittently penetrating the depth of the canopy coupled with differing spatially varying sources and/or sinks between the reactants. In low_soil_NO, no reactions have positive I_s greater than +5% aside from at the ground. In high_soil_NO, only three reactions have positive I_s greater than +10% above the ground: NO + NO_3, NO_2 + NO_3, and OH + NO_2.

In high_soil_NO, the most negative I_s in the canopy (and the largest absolute I_s out of all reactions) occurs for the reactions NO + XO_2 and NO + CH_3O_2 (ranging from −16% to −47% in the canopy). I_s for the reactions NO + XO_2 and NO + CH_3O_2 maximizes at 0.25h. I_s is also substantially negative for the reactions NO + ISOPBO_2, NO + ISOPAO_2, and O_3 + NO in the canopy. In low_soil_NO, negative I_s is largest above 0.75h for reaction between OH and isoprene. Below 0.75h, the reactions with the largest I_s are NO + XO_2, NO + CH_3O_2, O_3 + NO,

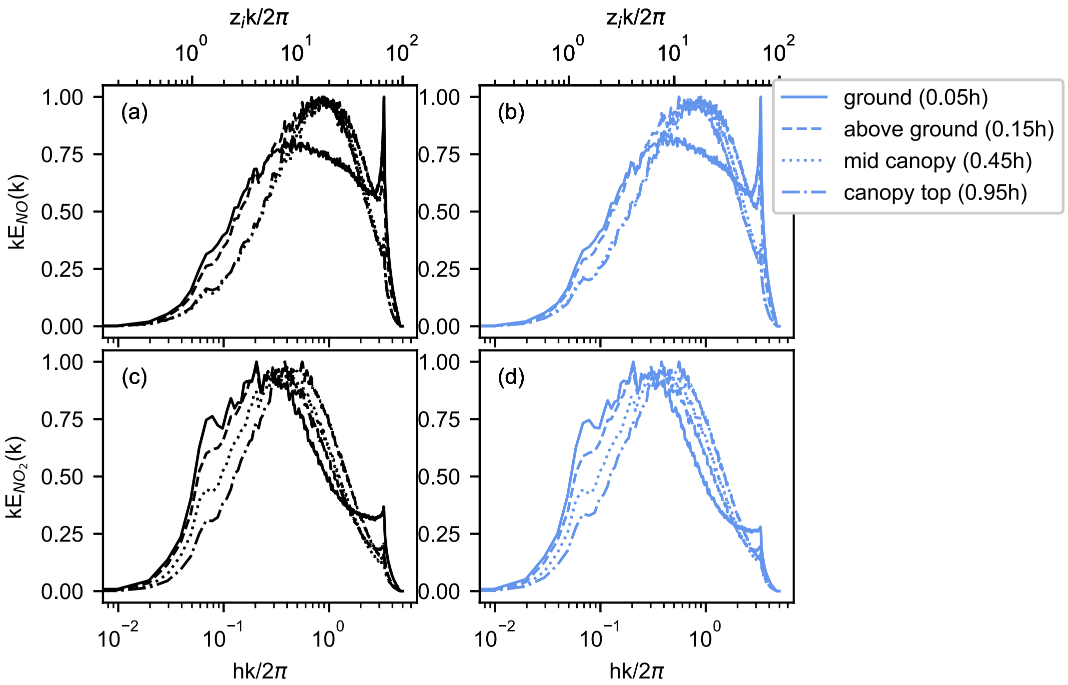

Figure 9. Azimuthally- and time-averaged two-dimensional spectra for NO (a, b) and NO_2 (c, d) at four heights in the canopy for low_soil_NO (a, c) and high_soil_NO (b, d). Because we aim to compare the shapes of the spectra across heights and not the absolute variability at a given height, each spectrum is normalized by its peak. Spectra are multiplied by horizontal wavenumber k such that the area under the curve is proportional to the total variance. The bottom x-axis is such that $x = 1$ is the scale of the canopy height (h), and the top x-axis is such that $x = 1$ is the scale of the ABL height (z_i).

NO + $ISOPAO_2$, NO + $ISOPBO_2$, and NO + NO_3. For these reactions except NO + NO_3, I_s increases substantially from low_soil_NO to high_soil_NO but remains the same sign. Excluding the reaction NO + NO_3, the reactions with high negative segregation in both cases are reactions between NO, which is emitted from the soil, and species that have large canopy sinks (i.e., O_3, XO_2, CH_3O_2, $ISOPAO_2$, $ISOPBO_2$; Figure 7).

For reaction between OH and isoprene, I_s is negative and up to −8% in high_soil_NO and −9% in low_soil_NO. In contrast to most other reactions, I_s for OH and isoprene maximizes at h. This is likely due to the peak in horizontal variability in isoprene at h; other reactants mostly have absolute peaks in their variability in the lower canopy (Figure S7 in Supporting Information S1).

In summary, segregation is highest in the canopy for heights up to 3h, and specifically at the ground for most reactions. Segregation is particularly important for reactions involving NO and NO_2. Reactions involving NO have greater than ±10% I_s somewhere in the canopy. Reactions involving NO_2 have greater than ±10% I_s somewhere in the canopy in high_soil_NO. The segregation of reactions involving NO and NO_2 mostly increase when soil NO emissions reflect the upper bound of observed values for temperate forests.

5.2. Understanding Segregation Changes With Height and High Versus Low Soil NO Emissions

Differences in I_s with species, height, and soil NO emissions only provide vague clues as to the controlling scales and thus processes. Given that we find that segregation is particularly important for reactions involving NO and NO_2, here we examine variability in NO and NO_2 and covariability in select reactions involving NO or NO_2 using spectral analysis in order to better understand the scales and processes controlling segregation.

5.2.1. Variability in NO and NO_2 Across Scales

Figure 9 shows the spectra of NO and NO_2 at different heights in the canopy. We already know that there are differences in the magnitude of variability in NO and NO_2 between the soil NO cases and with height (Figure 6 and Figure S7 in Supporting Information S1) so we normalize each spectrum by its highest value to isolate how the shape of the spectra, or the spatial character of variability, changes between cases and with height.

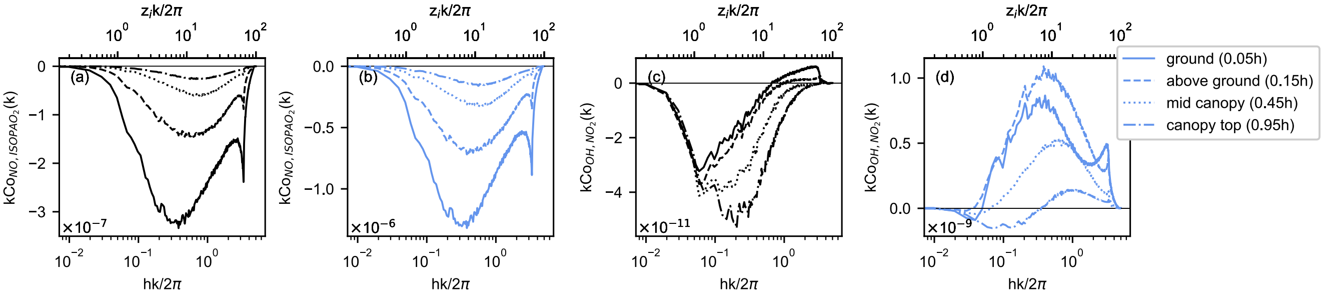

Figure 10. Azimuthally- and time-averaged two-dimensional co-spectra for the reactions NO + $ISOPAO_2$ and OH + NO_2 at four heights in the canopy for low_soil_NO (a, c) and high_soil_NO (b, d). Co-spectra are multiplied by horizontal wavenumber *k* such that the area under the curve is proportional to the total covariance. The bottom *x*-axis is such that $x = 1$ is the scale of the canopy height (*h*), and the top *x*-axis is such that $x = 1$ is the scale of the ABL height (z_i). The true y-values of the data are the numbers on the *y*-axes multiplied by the numbers in the lower left corner.

Between the soil NO cases, there is very little difference in the normalized NO and NO_2 spectra for a given height. There are, however, differences in the normalized NO and NO_2 spectra with height. First, there are thin spectral peaks at very high wavenumbers (i.e., corresponding to very small-scale processes) at and near the ground. Figure 9 shows that very small-scale processes are an important component of the variance for NO (less so for NO_2). Second, the spectra for NO and NO_2 near the ground are shifted to larger scales compared to higher in the canopy. NO_x variability near the ground may be more strongly influenced by the constant NO emission at the surface, which corresponds to the largest length scales in the domain. Thus, higher in the canopy, the spectral peaks shifting to smaller scales likely reflect a more dominant influence of fast chemistry on NO_x variability there, with a weakened role for NO emissions at the ground (and very small-scale processes).

That the normalized spectra are similar in shape between the soil NO cases at a given height suggests that the spatial character of the variation in NO and NO_2 remains the same between the cases. Similar spatial character in NO and NO_2 between cases despite changes in segregation in NO and NO_2 reactions implies that changes in the magnitude of variation in NO and NO_2 (Figure 6 and Figure S7 in Supporting Information S1) and/or how the NO and NO_2 change the spatial character or magnitude of variability in other quantities drives the differences in segregation between cases.

5.2.2. Select Reactions With High Segregation

Here we investigate I_s for select reactions by leveraging context from the co-spectra between reactants as well as the correlation coefficients between reactants and the individual reactant standard deviations. Note that the covariance between two quantities can be considered as the product of their correlation coefficient and the standard deviations in each quantity. We focus on two reactions that are important for photochemistry and have high segregation: OH + NO_2 and NO + $ISOPAO_2$. Figure 10 shows the absolute co-spectra at four heights in both cases (we show absolute co-spectra because we aim to discern how changes alter I_s). Figure 11 shows I_s and correlation coefficients for the reactions in both cases.

For NO + $ISOPAO_2$, we present evidence that changes in I_s with NO are largely due to the magnitude of NO variability. Changes with height are driven by the magnitude of NO and $ISOPAO_2$ variability. Our findings for the reaction NO + $ISOPAO_2$ are the same as for NO + $ISOPBO_2$, NO + CH_3O_2, NO + XO_2, and NO + O_3 (not shown), implying that there may be some generalizability about in-canopy segregation of reactant emitted at the ground versus reactants largely deposited to the canopy. Previous work suggests but does not show with interactive chemistry in an LES MLM that this may be the case (Edburg et al., 2012; Patton et al., 2001).

For OH + NO_2, changes in I_s with NO and height are influenced by changes in the magnitude of variability and/or spatial character of OH, as well as the magnitude of NO_2 variability. Generally, we find that low segregation above the canopy stems from low reactant variability, rather than a poor correlation between reactants (the correlations can be moderate to strong). Although it is challenging to determine what exactly drives changes in the correlation between reactants or in the magnitude of variability or spatial character of a given reactant, this analysis demonstrates that constraints on the distributions of reactants across scales in the canopy can aid in building mechanistic understanding of segregation changes with environmental conditions.

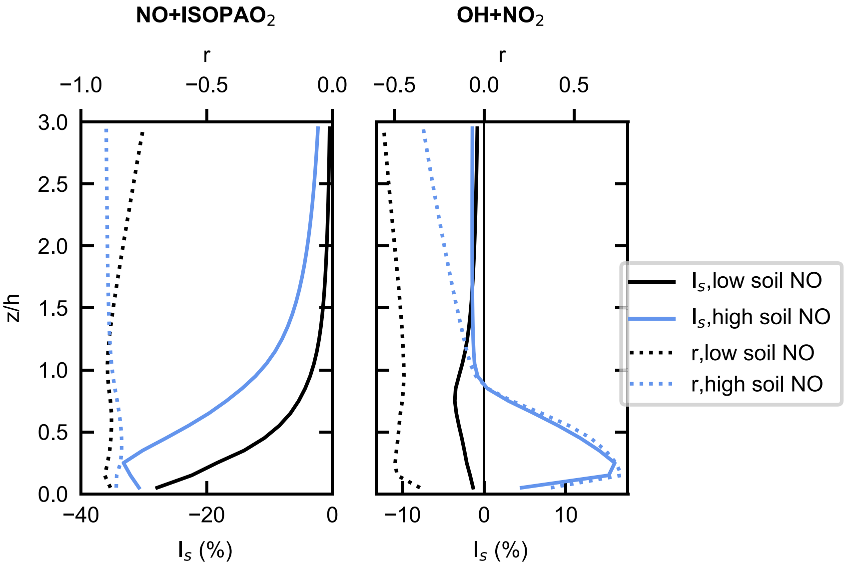

Figure 11. Vertical profiles from the ground to 3 *x* canopy height (*h*). Solid lines show intensities of segregation (I_s) for the reactions NO + ISOPAO$_2$ and OH + NO$_2$. Dotted lines show correlation coefficients (*r*) between reactants.

We first discuss the thin co-spectral peaks at high wavenumbers (i.e., that correspond to very small-scale processes). The peaks are especially apparent at the ground (Figure 10). Because there is high segregation at the ground, and we do not know what drives these peaks, we probe whether they drive the high segregation at the ground by calculating $\overline{X_1X_2}$ with low pass filtering of the reactant mixing ratios corresponding to an eddy turnover time of 10 s (a couple seconds longer than the very small-scale scales) for the reactions NO + ISOPAO$_2$ and OH + NO$_2$. At the ground, $\overline{X_1X_2}$ calculated with low pass filtering is within 1%–2% of $\overline{X_1X_2}$ calculated without low pass filtering. Thus, while these peaks may contribute to segregation, they do not drive the high segregation.

5.2.2.1. *NO + ISOPAO$_2$*

For the reaction NO + ISOPAO$_2$, I_s is negative and peaks in the lower canopy. The NO-ISOPAO$_2$ correlations do not have strong height variations, suggesting that vertical standard deviation profiles of NO and/or ISOPAO$_2$ (Figure S7 in Supporting Information S1) drive the vertical I_s profiles. Both reactants' variability peaks in the lower canopy, and thus both could contribute to height variation in I_s.

In terms of differences between cases, I_s is more strongly negative in high_soil_NO relative to low_soil_NO, with the difference decreasing with height. Together with the I_s difference between cases despite largely similar correlations between the cases, the similar-in-shape co-spectra at a given height between the cases (Figure 10) imply that the higher I_s from low_soil_NO to high_soil_NO stems from stronger reactant variability in high_soil_NO, rather than a different relationship between NO and ISOPAO$_2$ between the cases. While the standard deviations for ISOPAO$_2$ are slightly larger in high_soil_NO than low_soil_NO above the ground (by factor of 1.03–1.1), the increase in the standard deviation of NO (by a factor of 5–6) likely dominates the increase in I_s (Figure S7 in Supporting Information S1).

There may be more variability in NO with higher soil NO emissions simply because there is more NO. However, the coefficient of variation for NO increases substantially from low_soil_NO to high_soil_NO (from 15%–113% to 44%–173%), suggesting that the change in NO variability is not a simple function of the change in the amount of NO. The NO/NO$_2$ ratio changes such that more NO$_x$ is NO in high_soil_NO (Figure S6 in Supporting Information S1), which may play a role increasing relative NO variability.

5.2.2.2. *OH + NO$_2$*

For the reaction OH + NO$_2$, I_s below *h* is very different between cases, both in terms of sign and magnitude. Above *h*, I_s is small and positive in both cases. In this section, we first discuss in-canopy changes with height in low_soil_NO, then in-canopy changes with height in high_soil_NO, and finally differences between the cases at *h* and then in the canopy.

In low_soil_NO, I_s is negative and small below *h*, with a peak in the upper canopy. The highest I_s in the upper canopy likely reflects OH variability maximizing there (Figure S7 in Supporting Information S1) because the OH-NO_2 correlation is largely constant throughout the canopy (Figure 11) and NO_2 variability maximizes in the lower canopy (Figure S7 in Supporting Information S1). Additional evidence for a driving role for OH on changes in I_s with height for this case is that the co-spectra only increase with height at scales smaller than z_i, implying that the cause of the changes with height occurs at smaller scales (consistent with a role for OH because OH variability is largely driven by fast chemistry).

In high_soil_NO, I_s is positive below *h* and peaks strongly in the lower canopy. The co-spectra are mostly positive with the highest values just above the ground (but not at the ground), consistent with I_s maximizing in the lower canopy. The consistency of changes in height in I_s and the correlation suggests that changes in the relationship between OH and NO_2 with height drives changes in segregation with height in this case, but the vertical profile of variability in NO_2 (Figure S7 in Supporting Information S1) may also play a role. Regardless, this begs the question: why are the correlation and NO_2 variability strongest in lower canopy? To which, the answer may have to do with NO becoming a more important source of OH in high_soil_NO in the lower canopy (Figure S2 in Supporting Information S1).

At *h*, the co-spectra are different between cases. For example, on high_soil_NO at *h*, the co-spectrum is positive (like other heights) at small scales but is negative at large scales, which causes the overall correlation to become negative there. In low_soil_NO, the co-spectrum at *h* is negative at all scales. Despite differences between the cases in the co-spectra at *h* (as well as the correlation), I_s is similar and low, which may reflect reductions in OH and/or NO_2 variability at and above *h*.

Between the cases, large differences in shape and sign of the co-spectra are likely driven by differences in OH variability. There are not only strong changes in the magnitude of the OH standard deviation, but also the vertical profile of the OH standard deviation below 0.75*h* (Figure S7 in Supporting Information S1). In high_soil_NO, the OH standard deviation strongly peaks at the ground (in low_soil_NO the OH standard deviation peaks weakly at *h*). Together with the difference in the co-spectra between cases (and the correlation) despite similar NO_2 spatial character, the difference in the OH standard deviation vertical profile suggests a change in the OH spatial character as the underlying cause of the strong sign changes in OH-NO_2 segregation between cases.

We hypothesize that changes in the spatial character of OH between the soil NO cases result from the reaction HO_2 + NO becoming a much more important source of OH (Figure S2 in Supporting Information S1). Evidence includes a complete change in correlation coefficient between OH and NO in the canopy (Figure S8 in Supporting Information S1). The OH-NO correlation goes from negative and weak in low_soil_NO to positive and strong in high_soil_NO, which may be the result of an important source of OH from NO in high_soil_NO.

6. Comparison to Previous Work and Implications for Atmospheric Chemistry

In the context of key reactions for photochemistry, the reactions initiating oxidation are OH + CO and OH + CH_4 and OH + ISOP. While OH + CO and OH + CH_4 have very low I_s, negative I_s between OH and isoprene implies that chemistry following oxidation slows down relative to well-mixed conditions. The vertical profile and the magnitude of OH-ISOP I_s simulated here are similar to the Patton et al. (2001) estimates with simple proxies for OH and isoprene in a previous version of the NCAR-LES-MLM. However, our estimates are on the lower end of the Dlugi et al. (2010) estimates of −1 to −15% in the roughness sublayer of the forest (specifically, 7 m above canopy height) that employ 5-s measurements during the day at mixed forest in Germany during July 2003. Our estimates are also much lower than previous work estimating OH-ISOP I_s of up to −13% in a clear ABL using airborne measurements (Butler et al., 2008; Kaser et al., 2015). Other estimates with LES or airborne measurements suggests that heterogeneous isoprene emissions and clouds can alter OH-ISOP I_s (Brosse et al., 2018; Karl et al., 2007; Kaser et al., 2015; Kim et al., 2016; Krol et al., 2000; Li, Barth et al., 2016; Ouwersloot et al., 2011), but only clear-sky conditions and a canopy with homogenous structure and composition are investigated here.

In terms of changes with NO_x, we find that segregation between OH and isoprene is slightly stronger with lower soil NO. To our knowledge, only two studies probe changes in OH-ISOP I_s with changes in NO_x. With the Dutch Atmospheric Large-Eddy Simulation (DALES) simulating the ABL above a typical tropical forest, Ouwersloot et al. (2011) investigate the impact of an order of magnitude change in surface NO emissions (originally 0.5 ppt m s^{-1}), finding a very low impact on OH-ISOP I_s. However, in another set of sensitivity simulations, Ouwersloot et al. (2011) find increases in OH-ISOP I_s (factor of 1.6–1.7) with FT NO_2 increasing from 0 to 0.5 ppb. As simulated by the NCAR-LES-CHEM with updated version of the Horowitz et al. (2003) MOZART2.2 chemical mechanism by Kim et al. (2012) configured for a summer day in the southeast US, OH-ISOP I_s is negative and less than 10% near the surface but weakens (i.e., becomes closer to zero) as NO_x increases but remains less than 5 ppb (Kim et al., 2016). The I_s increase with lower NO_x is attributed to lower OH and thus higher isoprene and stronger variability (Kim et al., 2016). While we also find that I_s slightly increases with lower NO_x, isoprene variability is very similar between our soil NO cases. Thus, changes in OH variability or the OH-ISOP correlation likely drive differences. Future work will examine the causes and impacts of differences of OH-ISOP across our simulations.

Other reactions that are key for photochemistry include reactions between peroxy radicals (XO_2, CH_3O_2, $ISOPAO_2$, $ISOPBO_2$) and NO as well as reaction between OH and NO_2. Most previous work examining segregation examines isoprene and OH, but we find large negative I_s between peroxy radicals and NO, which implies a slowing down of the cycling of peroxy radicals with HO_x relative to well-mixed conditions. We also find segregation between OH and NO_2, which alters terminal loss of both HO_x and NO_x. When NO is lower, we find negative segregation between NO_2 and OH, which implies that there may be more NO_2 to photolyze to NO and ozone compared to well-mixed conditions. When NO is higher, there is positive segregation between NO_2 and OH, implying accelerated terminal loss and perhaps reduced ozone production relative to well-mixed conditions.

To estimate the impact of segregation on chemistry, we perform box-model simulations with our simplified mechanism similar to the simulations performed in Section 2.2.2. In a second simulation, we scale the rate coefficients by $(1 + I_s)$ for all reactions, with I_s simulated by the NCAR-LES-MLM-CHEM. We use I_s from $0.35h$ because segregation for most reactions maximizes around this height. Inserting the I_s from high_soil_NO into the polluted scenario (Figure S9 in Supporting Information S1), we find −3 to 3% relative changes in OH, but lower HO_2 (by −10.4% to −19.7%) and higher OH/HO_2 (by +8.5 to +28%). Ozone is lower by up to −2% (up to −1.2 ppb) when accounting for segregation. On the other hand, inserting the I_s from low_soil_NO into the clean scenario (Figure S10 in Supporting Information S1), we find +2.4 to +4.8% relative increases in OH and lower but then higher HO_2 (−4.2 to +3%) with mostly higher OH/HO_2 (up to +9.4%). Ozone is the same between simulations. In summary, while in both clean and polluted scenarios, segregation speeds up HO_x cycling, substantially, the effects on OH, HO_2, and ozone are different and can vary in sign between the scenarios. In general, differences in OH, HO_2, and ozone between the box model simulations with and without segregation implies that segregation may impact interpretations of observations and measurement-model comparisons.

7. Comparison to Previous Work and Implications for Ozone Dry Deposition

Observed ozone fluxes measured near the canopy top are commonly interpreted as dry deposition only but may be influenced by fast chemical losses of ozone such as the NO + O_3 reaction (Finco et al., 2018; Kramm et al., 1995; Plake et al., 2015). Negative NO-O_3 I_s means that the influence of NO on the ozone flux is even weaker than under the assumption of well-mixed conditions. To our knowledge, Edburg et al. (2012) is the only study to estimate NO-O_3 segregation in a canopy; however, they ignored the influence of chemistry. Using a previous version of the NCAR LES-MLM, with a sparser canopy and smaller domain, Edburg et al. (2012) estimate segregation between a scalar emitted from the ground (a proxy for NO) and a scalar deposited to the canopy (a proxy for ozone), finding I_s up to −8% in the canopy, with the largest segregation in the lower canopy and negligible above the canopy. Thus, in-canopy segregation is much larger in our simulations (up to −30% in the canopy), which likely result from interactive chemistry, interactive sources and sinks, and the larger domain size that allows ABL scales to influence turbulent transport in the canopy (Patton et al., 2016). The peak in the I_s vertical profile in Edburg et al. (2012) is also broader and occurs higher in the canopy than in our simulations; in addition to the other differences between our model configurations, this may also be due to the sparser canopy in Edburg et al. (2012) leading to more well-mixed air near the ground.

8. Conclusion

Previous work documents the NCAR-LES (e.g., Moeng, 1984; Moeng & Wyngaard, 1988; Sullivan et al., 1996) including the version coupled to a multilayer canopy model (Patton et al., 2016). We present a new version of the NCAR multilayer canopy LES coupled to a simplified chemical mechanism. We show that our mechanism can reproduce the features of first-generation isoprene chemistry and describe how we leverage a multi-species flux data set to parameterize dry deposition for all the gases in the mechanism. For the first time with both a vertically resolved and coupled forest and interactive chemistry in an LES, we demonstrate height-varying vertical profiles of reactant mixing ratios and fluxes as well as chemical segregation inside and above the canopy. We find large segregation for many reactions, in particular for reactions involving NO. Mostly reactant segregation is highest in the lower canopy and lowest above the canopy. With two simulations with differing soil NO emissions, we find that segregation generally becomes more important when soil NO emissions increase to the upper bound of observed values at temperate deciduous forests. For some reactions, segregation switches sign between low and high soil NO cases.

We use spectral analysis to gain a more complete understanding of the factors controlling reactant segregation. We show that not only are changes in the magnitude of reactant variability important for changes in segregation with soil NO emissions, but changes in the spatial character of reactants are important as well. However, capturing segregation accurately in our model requires a full understanding of reactant variability on fast timescales. Thus, there is a need for coupling model development with short-term field campaigns with simultaneous multi-height high-frequency observations of a variety of reactive gases' abundances and micrometeorology, as well as observational constraints on leaf and soil sources and sinks of reactants.

We close by emphasizing that our segregation estimates are closely tied to the atmospheric configuration and chemical mechanism. Changes to the atmospheric configuration will change the character of the organized structures within the turbulence, and changes to the chemical mechanism will alter the pathways by which species are transformed. With access to sufficient computational time, the model introduced here can be expanded to include more reactants and/or a more complex chemical mechanism and simulate other environments (e.g., different atmospheric stability, forest type, chemical composition, and clouds). Such simulations will be key for advancing predictive ability of turbulence-chemistry interactions at regional-to-global scales.

Data Availability Statement

Processed data from the LES is provided in the NCAR Geoscience Data Exchange repository (https://doi.org/10.5065/ky81-f733).

Acknowledgments
This material is based upon work supported by the National Center for Atmospheric Research, which is a major facility sponsored by the National Science Foundation under Cooperative Agreement No. 1852977. We acknowledge high-performance computing support from Cheyenne (http://dx.doi.org/10.5065/D6R129HX) provided by NCAR's Computational and Information Systems Laboratory, sponsored by the National Science Foundation. We thank Steve Oncley for providing the observed radiation profiles. S. W. and R. H. S. were supported in part by the NOAA Cooperative Agreement with CIRES, NA17OAR4320101. We thank two anonymous reviewers for their constructive comments of our manuscript.

References

Arneth, A., Harrison, S. P., Zaehle, S., Tsigaridis, K., Menon, S., Bartlein, P. J., et al. (2011). Terrestrial biogeochemical feedbacks in the climate system. *Nature Geoscience*, *3*(8), 525–532. https://doi.org/10.1038/NGEO905

Ashworth, K., Chung, S. H., Griffin, R. J., Chen, J., Forkel, R., Bryan, A. M., & Steiner, A. L. (2015). FORest Canopy Atmosphere Transfer (FORCAsT) 1.0: A 1-D model of biosphere-atmosphere chemical exchange. *Geoscientific Model Development*, *8*(11), 3765–3784. https://doi.org/10.5194/gmd-8-3765-2015

Atkinson, R., Baulch, D. L., Cox, R. A., Crowley, J. N., Hampson, R. F., Hynes, R. G., et al. (2004). Evaluated kinetic and photochemical data for atmospheric chemistry: Volume I—Gas phase reactions of O_x, HO_x, NO_x and SO_x species. *Atmospheric Chemistry and Physics*, *4*(6), 1461–1738. https://doi.org/10.5194/acp-4-1461-2004

Atkinson, R., Baulch, D. L., Cox, R. A., Crowley, J. N., Hampson, R. F., Hynes, R. G., et al. (2006). Evaluated kinetic and photochemical data for atmospheric chemistry: Volume II—Gas phase reactions of organic species. *Atmospheric Chemistry and Physics*, *6*(11), 3625–4055. https://doi.org/10.5194/acp-6-3625-2006

Ball, J. T., Woodrow, I. E., & Berry, J. A. (1987). A model predicting stomatal conductance and its contribution to the control of photosynthesis under different environmental conditions. In J. Biggens (Ed.), *Progress in photosynthesis research* (pp. 221–224). Martinus Nijhoff.

Barth, M., McFadden, J. P., Sun, J., Wiedinmyer, C., Chuang, P., Collins, D., et al. (2005). Coupling between land ecosystems and the atmospheric hydrologic cycle through biogenic aerosol pathways. *Bulletin of the American Meteorological Society*, *86*(12), 1738–1742. https://doi.org/10.1175/bams-86-12-1738

Bates, K. H., & Jacob, D. J. (2019). A new model mechanism for atmospheric oxidation of isoprene: Global effects on oxidants, nitrogen oxides, organic products, and secondary organic aerosol. *Atmospheric Chemistry and Physics*, *19*(14), 9613–9640. https://doi.org/10.5194/acp-19-9613-2019

Bauer, M. R., Hultman, N. E., Panek, J. A., & Goldstein, A. H. (2000). Ozone deposition to a ponderosa pine plantation in the Sierra Nevada Mountains (CA): A comparison of two different climatic years. *Journal of Geophysical Research*, *105*(D17), 22123–22136. https://doi.org/10.1029/2000JD900168

Brosse, F., Leriche, M., Mari, C., & Couvreux, F. (2018). LES study of the impact of moist thermals on the oxidative capacity of the atmosphere in southern West Africa. *Atmospheric Chemistry and Physics*, *18*(9), 6601–6624. https://doi.org/10.5194/acp-18-6601-2018

Brown, P. N., Byrne, G. D., & Hindmarsh, A. C. (1989). VODE, a variable-coefficient ODE solver. *SIAM Journal on Scientific and Statistical Computing*, *10*(5), 1038–1051. https://doi.org/10.1137/0910062

Brunet, Y. (2020). Turbulent flow in plant canopies: Historical perspective and overview. *Boundary-Layer Meteorology*, *177*(2–3), 315–364. https://doi.org/10.1007/s10546-020-00560-7

Bryan, A. M., Bertman, S. B., Carroll, M. A., Dusanter, S., Edwards, G. D., Forkel, R., et al. (2012). In-canopy gas-phase chemistry during CABINEX 2009: Sensitivity of a 1-D canopy model to vertical mixing and isoprene chemistry. *Atmospheric Chemistry and Physics*, *12*(18), 8829–8849. https://doi.org/10.5194/acp-12-8829-2012

Burkhardt, J., & Eiden, R. (1994). Thin water films on coniferous needles. *Atmospheric Environment*, *28*(12), 2001–2011. https://doi.org/10.1016/1352-2310(94)90469-3

Burkhardt, J., & Hunsche, M. (2013). "Breath figures" on leaf surfaces—Formation and effects of microscopic leaf wetness. *Frontiers of Plant Science*, *4*(422). https://doi.org/10.3389/fpls.2013.00422

Burkholder, J. B., Sander, S. P., Abbatt, J., Barker, J. R., Huie, R. E., Kolb, C. E., et al. (2015). *Chemical kinetics and photochemical data for use in atmospheric studies evaluation no. 18 (JPL Publication 15-10)*. Jet Propulsion Laboratory.

Butler, T. M., Taraborrelli, D., Brühl, C., Fischer, H., Harder, H., Martinez, M., et al. (2008). Improved simulation of isoprene oxidation chemistry with the ECHAM5/MESSy chemistry-climate model: Lessons from the GABRIEL airborne field campaign. *Atmospheric Chemistry and Physics*, *8*(16), 4529–4546. https://doi.org/10.5194/acp-8-4529-2008

Carlton, A. G., de Gouw, J., Jimenez, J. L., Ambrose, J. L., Attwood, A. R., Brown, S., et al. (2018). Synthesis of the southeast atmosphere studies: Investigating fundamental atmospheric chemistry questions. *Bulletin of the American Meteorological Society*, *99*(3), 547–567. https://doi.org/10.1175/BAMS-D-16-0048.1

Chaparro-Suarez, I. G., Meixner, F. X., & Kesselmeier, J. (2011). Nitrogen dioxide (NO_2) uptake by vegetation controlled by atmospheric concentrations and plant stomatal aperture. *Atmospheric Environment*, *45*(32), 5742–5750. https://doi.org/10.1016/j.atmosenv.2011.07.021

Chen, F., Manning, K. W., LeMone, M. A., Trier, S. B., Alfieri, J. G., Roberts, R., et al. (2007). Description and evaluation of the characteristics of the NCAR high-resolution land data assimilation system. *Journal of Applied Meteorology and Climatology*, *46*(6), 694–713. https://doi.org/10.1175/JAM2463.1

Clifton, O. E., Fiore, A. M., Massman, W. J., Baublitz, C. B., Coyle, M., Emberson, L., et al. (2020). Dry deposition of ozone over land: Processes, measurement, and modeling. *Reviews of Geophysics*, *58*(1), e2019RG000670. https://doi.org/10.1029/2019RG000670

Clifton, O. E., Fiore, A. M., Munger, J. W., Malyshev, S., Horowitz, L. W., Shevliakova, E., et al. (2017). Interannual variability in ozone removal by a temperate deciduous forest. *Geophysical Research Letters*, *44*(1), 542–552. https://doi.org/10.1002/2016GL070923

Clifton, O. E., Fiore, A. M., Munger, J. W., & Wehr, R. (2019). Spatiotemporal controls on observed daytime ozone deposition velocity over Northeastern U.S. forests during summer. *Journal of Geophysical Research: Atmospheres*, *124*(10), 5612–5628. https://doi.org/10.1029/2018JD029073

Clifton, O. E., & Patton, E. G. (2021). Does organization in turbulence influence ozone removal by deciduous forests? *Journal of Geophysical Research: Biogeosciences*, *126*(6), e2021JG006362. https://doi.org/10.1029/2021JG006362

Crounse, J. D., Paulot, F., Kjaergaard, H. G., & Wennberg, P. O. (2011). Peroxy radical isomerization in the oxidation of isoprene. *Physical Chemistry Chemical Physics*, *13*(30), 13607–13613. https://doi.org/10.1039/C1CP21330J

Crutzen, P. J. (1974). Photochemical reactions initiated by and influencing ozone in unpolluted tropospheric air. *Tellus*, *26*(1–2), 47–57. https://doi.org/10.1111/j.2153-3490.1974.tb01951.x

Crutzen, P. J. (1979). The role of NO and NO_2 in the chemistry of the troposphere and stratosphere. *Annual Review of Earth and Planetary Sciences*, *7*(1), 443–472. https://doi.org/10.1146/annurev.ea.07.050179.002303

Damian, V., Sandu, A., Damian, M., Potra, F., & Carmichael, G. R. (2002). The Kinetic PreProcessor KPP -- A Software Environment for Solving Chemical Kinetics. *Computers and Chemical Engineering*, *26*(11), 1567–1579.

Deardorff, J. W. (1980). Stratocumulus-capped mixed layers derived from a three-dimensional model. *Boundary-Layer Meteorology*, *18*(4), 495–527. https://doi.org/10.1007/BF00119502

Delaria, E. R., Place, B. K., Liu, A. X., & Cohen, R. C. (2020). Laboratory measurements of stomatal NO_2 deposition to native California trees and the role of forests in the NO_x cycle. *Atmospheric Chemistry and Physics*, *20*(22), 14023–14041. https://doi.org/10.5194/acp-20-14023-2020

Delaria, E. R., Vieira, M., Cremieux, J., & Cohen, R. C. (2018). Measurements of NO and NO_2 exchange between the atmosphere and *Quercus agrifolia*. *Atmospheric Chemistry and Physics*, *18*(19), 14161–14173. https://doi.org/10.5194/acp-18-14161-2018

DiGangi, J. P., Boyle, E. S., Karl, T., Harley, P., Turnipseed, A., Kim, S., et al. (2011). First direct measurements of formaldehyde flux via eddy covariance: Implications for missing in-canopy formaldehyde sources. *Atmospheric Chemistry and Physics*, *11*(20), 10565–10578. https://doi.org/10.5194/acp-11-10565-2011

Dlugi, R., Berger, M., Zelger, M., Hofzumahaus, A., Siese, M., Holland, F., et al. (2010). Turbulent exchange and segregation of HO_x radicals and volatile organic compounds above a deciduous forest. *Atmospheric Chemistry and Physics*, *10*(13), 6215–6235. https://doi.org/10.5194/acp-10-6215-2010

Dupont, S., & Patton, E. G. (2012). Influence of stability and seasonal canopy changes on micrometeorology within and above an orchard canopy: The CHATS experiment. *Agricultural and Forest Meteorology*, *157*, 11–29. https://doi.org/10.1016/j.agrformet.2012.01.011

Edburg, S. L., Stock, D., Lamb, B. K., & Patton, E. G. (2012). The effect of the vertical source distribution on scalar statistics within and above a forest canopy. *Boundary-Layer Meteorology*, *142*(3), 365–382. https://doi.org/10.1007/s10546-011-9686-1

Eiden, R., Burkhardt, J., & Burkhardt, O. (1994). Atmospheric aerosol particles and their role in the formation of dew on the surface of plant leaves. *Journal of Aerosol Science*, *25*(2), 367–376. https://doi.org/10.1016/0021-8502(94)90087-6

Emmons, L. K., Schwantes, R. H., Orlando, J. J., Tyndall, G., Kinnison, D., Lamarque, J.-F., et al. (2020). The chemistry mechanism in the community earth system model version 2 (CESM2). *Journal of Advances in Modeling Earth Systems*, *12*(4), e2019MS001882. https://doi.org/10.1029/2019MS001882

Emmons, L. K., Walters, S., Hess, P. G., Lamarque, J. F., Pfister, G. G., Fillmore, D., et al. (2010). Description and evaluation of the model for ozone and related chemical tracers, version 4 (MOZART-4). *Geoscientific Model Development*, *3*(1), 43–67. https://doi.org/10.5194/gmd-3-43-2010

Farmer, D. K., & Riches, M. (2020). Measuring biosphere–atmosphere exchange of short-lived climate forcers and their precursors. *Accounts of Chemical Research*, *53*(8), 1427–1435. https://doi.org/10.1021/acs.accounts.0c00203

Fehsenfeld, F., Calvert, J., Fall, R., Goldan, P., Guenther, A. B., Nicholas Hewitt, C., et al. (1992). Emissions of volatile organic compounds from vegetation and the implications for atmospheric chemistry. *Global Biogeochemical Cycles*, *6*(4), 389–430. https://doi.org/10.1029/92GB02125

Filella, I., Peñuelas, J., & Llusià, J. (2006). Dynamics of the enhanced emissions of monoterpenes and methyl salicylate, and decreased uptake of formaldehyde, by *Quercus ilex* leaves after application of jasmonic acid. *New Phytologist*, *169*(1), 135–144. https://doi.org/10.1111/j.1469-8137.2005.01570.x

Finco, A., Coyle, M., Nemitz, E., Marzuoli, R., Chiesa, M., Loubet, B., et al. (2018). Characterization of ozone deposition to mixed oak-hornbeam forest—Flux measurements at five levels above and inside the canopy and their interactions with nitric oxide. *Atmospheric Chemistry and Physics*, *18*(24), 17945–17961. https://doi.org/10.5194/acp-18-17945-2018

Finkelstein, P. L., Ellestad, T. G., Clarke, J. F., Meyers, T. P., Schwede, D. B., Hebert, E. O., & Neal, J. A. (2000). Ozone and sulfur dioxide dry deposition to forests: Observations and model evaluation. *Journal of Geophysical Research*, *105*(D12), 15365–15377. https://doi.org/10.1029/2000JD900185

Finnigan, J. J., Shaw, R. H., & Patton, E. G. (2009). Turbulence structure above a vegetation canopy. *Journal of Fluid Mechanics*, *637*, 387–424. https://doi.org/10.1017/S0022112009990589

Fiore, A. M., Naik, V., Spracklen, D. V., Steiner, A., Unger, N., Prather, M., et al. (2012). Global air quality and climate. *Chemical Society Reviews*, *41*(19), 6663–6683. https://doi.org/10.1039/c2cs35095e

Forkel, R., Klemm, O., Graus, M., Rappenglück, B., Stockwell, W. R., Grabmer, W., et al. (2006). Trace gas exchange and gas phase chemistry in a Norway spruce forest: A study with a coupled 1-dimensional canopy atmospheric chemistry emission model. *Atmospheric Environment*, *40*, 28–42. https://doi.org/10.1016/j.atmosenv.2005.11.070

Fowler, D., Pilegaard, K., Sutton, M. A., Ambus, P., Raivonen, M., Duyzer, J., et al. (2009). Atmospheric composition change: Ecosystems-atmosphere interactions. *Atmospheric Environment*, *43*(33), 5193–5267. https://doi.org/10.1016/j.atmosenv.2009.07.068

Fuentes, J. D., Gerken, T., Chamecki, M., Stoy, P., Freire, L., & Ruiz-Plancarte, J. (2022). Turbulent transport and reactions of plant-emitted hydrocarbons in an Amazonian rain forest. *Atmospheric Environment*, *279*, 119094. https://doi.org/10.1016/j.atmosenv.2022.119094

Fumagalli, I., Gruening, C., Marzuoli, R., Cieslik, S., & Gerosa, G. (2016). Long-term measurements of NO_x and O_3 soil fluxes in a temperate deciduous forest. *Agricultural and Forest Meteorology*, *228*, 205–216. https://doi.org/10.1016/j.agrformet.2016.07.011

Galloway, M. M., DiGangi, J. P., Hottle, J. R., Huisman, A. J., Mielke, L. H., Alaghmand, M., et al. (2012). Observations and modeling of formaldehyde at the PROPHET mixed hardwood forest site in 2008. *Atmospheric Environment*, *49*, 403–410. https://doi.org/10.1016/j.atmosenv.2011.09.053

Ganzeveld, L. N., Lelieveld, J., Dentener, F. J., Krol, M. C., & Roelofs, G. J. (2002). Atmosphere-biosphere trace gas exchanges simulated with a single-column model. *Journal of Geophysical Research*, *107*(D16), 4297. https://doi.org/10.1029/2001JD000684

Gao, W., Shaw, R. H., & Paw, U. K. T. (1989). Observation of organized structure in turbulent flow within and above a forest canopy. *Boundary-Layer Meteorology*, *47*(1–4), 349–377. https://doi.org/10.1007/BF00122339

Gao, W., Shaw, R. H., & Paw, U. K. T. (1992). Conditional analysis of temperature and humidity microfronts and ejection/sweep motions within and above a deciduous forest. *Boundary-Layer Meteorology*, *59*(1–2), 35–57. https://doi.org/10.1007/BF00120685

Gao, W., Wesely, M. L., & Doskey, P. V. (1993). Numerical modeling of the turbulent-diffusion and chemistry of NO_x, O_3, isoprene, and other reactive trace gases in and above a forest canopy. *Journal of Geophysical Research*, *98*(D10), 18339–18353. https://doi.org/10.1029/93jd01862

Goldstein, A. H., Goulden, M. L., Munger, J. W., Wofsy, S. C., & Geron, C. D. (1998). Seasonal course of isoprene emissions from a midlatitude deciduous forest. *Journal of Geophysical Research*, *103*(D23), 31045–31056. https://doi.org/10.1029/98jd02708

Gray, C. M., Monson, R. K., & Fierer, N. (2014). Biotic and abiotic controls on biogenic volatile organic compound fluxes from a subalpine forest floor. *Journal of Geophysical Research: Biogeosciences*, *119*(4), 547–556. https://doi.org/10.1002/2013JG002575

Guenther, A., Baugh, B., Brasseur, G., Greenberg, J., Harley, P., Klinger, L., et al. (1999). Isoprene emission estimates and uncertainties for the Central African EXPRESSO study domain. *Journal of Geophysical Research*, *104*(D23), 30625–30639. https://doi.org/10.1029/1999JD900391

Guenther, A., Hewitt, C. N., Erickson, D., Fall, R., Geron, C., Graedel, T., et al. (1995). A global model of natural volatile organic compound emissions. *Journal of Geophysical Research*, *100*(D5), 8873–8892. https://doi.org/10.1029/94JD02950

Guenther, A., Karl, T., Harley, P., Wiedinmyer, C., Palmer, P. I., & Geron, C. (2006). Estimates of global terrestrial isoprene emissions using MEGAN (Model of Emissions of Gases and Aerosols from Nature). *Atmospheric Chemistry and Physics*, *6*(11), 3181–3210. https://doi.org/10.5194/acp-6-3181-2006

Guenther, A. B., Jiang, X., Heald, C. L., Sakulyanontvittaya, T., Duhl, T., Emmons, L. K., & Wang, X. (2012). The model of emissions of gases and aerosols from nature version 2.1 (MEGAN2.1): An extended and updated framework for modeling biogenic emissions. *Geoscientific Model Development*, *5*(6), 1471–1492. https://doi.org/10.5194/gmd-5-1471-2012

Hallquist, M., Wenger, J. C., Baltensperger, U., Rudich, Y., Simpson, D., Claeys, M., et al. (2009). The formation, properties and impact of secondary organic aerosol: Current and emerging issues. *Atmospheric Chemistry and Physics*, *9*(14), 5155–5236. https://doi.org/10.5194/acp-9-5155-2009

Hardacre, C., Mulcahy, J. P., Pope, R. J., Jones, C. G., Rumbold, S. R., Li, C., et al. (2021). Evaluation of SO_2, SO_4^{2-} and an updated SO_2 dry deposition parameterization in UKESM1. *Atmospheric Chemistry and Physics*, *21*(24), 18465–18467. https://doi.org/10.5194/acp-21-18465-2021

He, C., Clifton, O., Felker-Quinn, E., Fulgham, S. R., Juncosa Calahorrano, J., Lombardozzi, D., et al. (2021). Interactions between air pollution and terrestrial ecosystems: Perspectives on challenges and future directions. *Bulletin of the American Meteorological Society*, *102*(3), E525–E538. https://doi.org/10.1175/BAMS-D-20-0066.1

Helmig, D., Greenberg, J., Guenther, A., Zimmerman, P., & Geron, C. (1998). Volatile organic compounds and isoprene oxidation products at a temperate deciduous forest site. *Journal of Geophysical Research*, *103*(D17), 22397–22414. https://doi.org/10.1029/98JD00969

Henze, D. K., & Seinfeld, J. H. (2006). Global secondary organic aerosol from isoprene oxidation. *Geophysical Research Letters*, *33*(9), L09812. https://doi.org/10.1029/2006GL025976

Horowitz, L. W., Walters, S., Mauzerall, D. L., Emmons, L. K., Rasch, P. J., Granier, C., et al. (2003). A global simulation of tropospheric ozone and related tracers: Description and evaluation of MOZART, version 2. *Journal of Geophysical Research*, *108*(D24), 4784. https://doi.org/10.1029/2002JD002853

Jacob, D. J., & Bakwin, P. S. (1991). Cycling of NO_x in tropical forest canopies. In J. E. Rogers & W. B. Whitman (Eds.), *Microbial production and consumption of greenhouse gases: Methane, nitrogen oxides, and halomethanes* (pp. 237–253). American Society for Microbiology.

Jarvis, P. G. (1976). The interpretation of the variations in leaf water potential and stomatal conductance found in canopies in the field. *Philosophical Transactions of the Royal Society of London: Series B, Biological Sciences*, *273*, 593–610.

Jenkin, M. E., Young, J. C., & Rickard, A. R. (2015). The MCM v3.3.1 degradation scheme for isoprene. *Atmospheric Chemistry and Physics*, *15*(20), 11433–11459. https://doi.org/10.5194/acp-15-11433-2015

Kanda, M., & Hino, M. (1994). Organized structures in developing turbulent flow within and above a plant canopy, using a large eddy simulation. *Boundary-Layer Meteorology*, *68*(3), 237–257. https://doi.org/10.1007/BF00705599

Karl, T., Guenther, A., Yokelson, R. J., Greenberg, J., Potosnak, M., Blake, D. R., & Artaxo, P. (2007). The tropical forest and fire emissions experiment: Emission, chemistry, and transport of biogenic volatile organic compounds in the lower atmosphere over Amazonia. *Journal of Geophysical Research*, *112*(D18), D18302. https://doi.org/10.1029/2007JD008539

Karl, T., Harley, P., Emmons, L., Thornton, B., Guenther, A., Basu, C., et al. (2010). Efficient atmospheric cleansing of oxidized organic trace gases by vegetation. *Science*, *330*(6005), 816–819. https://doi.org/10.1126/science.1192534

Kaser, L., Karl, T., Yuan, B., Mauldin, R. L., Cantrell, C. A., Guenther, A. B., et al. (2015). Chemistry-turbulence interactions and mesoscale variability influence the cleansing efficiency of the atmosphere. *Geophysical Research Letters*, *42*(24), 10894–10903. https://doi.org/10.1002/2015GL066641

Kim, S.-W., Barth, M. C., & Trainer, M. (2012). Influence of fair weather cumulus clouds on isoprene chemistry. *Journal of Geophysical Research*, *117*(D10), D10302. https://doi.org/10.1029/2011JD017099

Kim, S.-W., Barth, M. C., & Trainer, M. (2016). Impact of turbulent mixing on isoprene chemistry. *Geophysical Research Letters*, *43*(14), 7701–7708. https://doi.org/10.1002/2016gl069752

Knote, C., Hodzic, A., & Jimenez, J. L. (2015). The effect of dry and wet deposition of condensable vapors on secondary organic aerosols concentrations over the continental US. *Atmospheric Chemistry and Physics*, *15*, 1–18. https://doi.org/10.5194/acp-15-1-2015

Kramm, G., Dlugi, R., Dollard, G. J., Foken, T., Mölders, N., Müller, H., et al. (1995). On the dry deposition of ozone and reactive nitrogen species. *Atmospheric Environment*, *29*(21), 3209–3231. https://doi.org/10.1016/1352-2310(95)00218-n

Kramshøg, M., Albers, C. N., Holst, T., Holzinger, R., Elberling, B., & Rinnan, R. (2018). Biogenic volatile release from permafrost thaw is determined by the soil microbial sink. *Nature Communications*, *9*(1), 3412. https://doi.org/10.1038/s41467-018-05824-y

Krol, M. C., Molemaker, M. J., & de Arellano, J. V. (2000). Effects of turbulence and heterogeneous emissions on photochemically active species in the convective boundary layer. *Journal of Geophysical Research*, *105*(D5), 6871–6884. https://doi.org/10.1029/1999jd900958

Laisk, A., Kull, O., & Moldau, H. (1989). Ozone concentration in leaf intercellular air spaces is close to zero. *Plant Physiology*, *90*(3), 1163–1167. https://doi.org/10.1104/pp.90.3.1163

Lenschow, D. H., Gurarie, D., & Patton, E. G. (2016). Modeling the diurnal cycle of conserved and reactive species in the convective boundary layer using SOMCRUS. *Geoscientific Model Development*, *9*(3), 979–996. https://doi.org/10.5194/gmd-9-979-2016

Leuning, R., Kelliher, F. M., De Pury, D. G. G., & Schulze, E.-D. (1995). Leaf nitrogen, photosynthesis, conductance and transpiration: Scaling from leaves to canopies. *Plant, Cell and Environment*, *18*(10), 1183–1200. https://doi.org/10.1111/j.1365-3040.1995.tb00628.x

Levy, H., II (1971). Normal atmosphere: Large radical and formaldehyde concentrations predicted. *Science*, *173*(3992), 141–143. https://doi.org/10.1126/science.173.3992.141

Li, G., Su, H., Li, X., Kuhn, U., Meusel, H., Hoffmann, T., et al. (2016). Uptake of gaseous formaldehyde by soil surfaces: A combination of adsorption/desorption equilibrium and chemical reactions. *Atmospheric Chemistry and Physics*, *16*(15), 10299–10311. https://doi.org/10.5194/acp-16-10299-2016

Li, Y., Barth, M. C., Chen, G., Patton, E. G., Kim, S.-W., Wisthaler, A., et al. (2016). Large-eddy simulation of biogenic VOC chemistry during the DISCOVER-AQ 2011 campaign. *Journal of Geophysical Research: Atmospheres*, *121*(13), 8083–8105. https://doi.org/10.1002/2016JD024942

Li, Y., Barth, M. C., Patton, E. G., & Steiner, A. L. (2017). Impact of in-cloud aqueous processes on the chemistry and transport of biogenic volatile organic compounds. *Journal of Geophysical Research: Atmospheres*, *122*(20), 11131–11153. https://doi.org/10.1002/2017JD026688

Ma, Y., & Liu, H. (2019). An advanced multiple-layer canopy model in the WRF model with large-eddy simulations to simulate canopy flows and scalar transport under different stability conditions. *Journal of Advances in Modeling Earth Systems*, *11*(7), 2330–2351. https://doi.org/10.1029/2018MS001347

Mao, J., Carlton, A., Cohen, R. C., Brune, W. H., Brown, S. S., Wolfe, G. M., et al. (2018). Southeast Atmosphere studies: Learning from model-observation syntheses. *Atmospheric Chemistry and Physics*, *18*(4), 2615–2651. https://doi.org/10.5194/acp-18-2615-2018

Massman, W. J. (2004). Toward an ozone standard to protect vegetation based on effective dose: A review of deposition resistances and a possible metric. *Atmospheric Environment*, *38*(15), 2323–2337. https://doi.org/10.1016/j.atmosenv.2003.09.079

McKinney, K. A., Lee, B. H., Vasta, A., Pho, T. V., & Munger, J. W. (2011). Emissions of isoprenoids and oxygenated biogenic volatile organic compounds from a New England mixed forest. *Atmospheric Chemistry and Physics*, *11*(10), 4807–4831. https://doi.org/10.5194/acp-11-4807-2011

Mikkelsen, T. N., Ro-Poulsen, H., Hovmand, M. F., Jensen, N. O., Pilegaard, K., & Egeløv, A. H. (2004). Five-year measurements of ozone fluxes to a Danish Norway spruce canopy. *Atmospheric Environment*, *38*(15), 2361–2371. https://doi.org/10.1016/j.atmosenv.2003.12.036

Moeng, C.-H. (1984). A large-eddy-simulation model for the study of planetary boundary-layer turbulence. *Journal of the Atmospheric Sciences*, *41*(13), 2052–2062. https://doi.org/10.1175/1520-0469(1984)041<2052:alesmf>2.0.co;2

Moeng, C.-H., & Sullivan, P. P. (1994). A comparison of shear-and buoyancy-driven planetary boundary layer flows. *Journal of the Atmospheric Sciences*, *51*(7), 999–1022. https://doi.org/10.1175/1520-0469(1994)051<0999:acosab>2.0.co;2

Moeng, C.-H., & Wyngaard, J. C. (1988). Spectral analysis of large-eddy simulations of the convective boundary layer. *Journal of the Atmospheric Sciences*, *45*(23), 3573–3587. https://doi.org/10.1175/1520-0469(1988)045<3573:saoles>2.0.co;2

Monteith, J. L., & Unsworth, M. H. (1990). *Principles of Environmental Physics* (2nd ed.). Edward Arnold.

Moon, Z., Fuentes, J. D., & Staebler, R. M. (2020). Impacts of spectrally resolved irradiance on photolysis frequency calculations within a forest canopy. *Agricultural and Forest Meteorology*, *291*, 108012. https://doi.org/10.1016/j.agrformet.2020.108012

Neirynck, J., & Verstraeten, A. (2018). Variability of ozone deposition velocity over a mixed Suburban temperate forest. *Frontiers in Environmental Science*, *6*, 82. https://doi.org/10.3389/fenvs.2018.00082

Nguyen, T. B., Crounse, J. D., Teng, A. P., Clair, J. M., Paulot, F., Wolfe, G. M., & Wennberg, P. O. (2015). Rapid deposition of oxidized biogenic compounds to a temperate forest. *Proceedings of the National Academy of Sciences*, *112*(5), E392–E401. https://doi.org/10.1073/pnas.1418702112

Niinemets, Ü., Fares, S., Harley, P., & Jardine, K. J. (2014). Bidirectional exchange of biogenic volatiles with vegetation: Emission sources, reactions, breakdown and deposition. *Plant, Cell and Environment*, *37*(8), 1790–1809. https://doi.org/10.1111/pce.12322

Nikolov, N. T., Massman, W. J., & Schoettle, A. W. (1995). Coupling biochemical and biophysical processes at the leaf level: An equilibrium photosynthesis model for leaves of C_3 plants. *Ecological Modeling*, *80*(2–3), 205–235. https://doi.org/10.1016/0304-3800(94)00072-P

Nobel, P. S. (1991). *Physiochemical and environmental plant physiology* (1st ed.). Academic Press, Inc.

Omasa, K., Tobe, K., Hosomi, M., & Kobayashi, M. (2000). Absorption of ozone and seven organic pollutants by Populus nigra and Camellia sasanqua. *Environmental Science & Technology*, *34*(12), 2498–2500. https://doi.org/10.1021/es991285m

Ouwersloot, H. G., Vilà-Guerau de Arellano, J., van Heerwaarden, C. C., Ganzeveld, L. N., Krol, M. C., & Lelieveld, J. (2011). On the segregation of chemical species in a clear boundary layer over heterogeneous land surfaces. *Atmospheric Chemistry and Physics*, *11*(20), 10681–10704. https://doi.org/10.5194/acp-11-10681-2011

Patton, E. G., Davis, K. J., Barth, M. C., & Sullivan, P. P. (2001). Decaying scalars emitted by a forest canopy: A numerical study. *Boundary-Layer Meteorology*, *100*(1), 91–129. https://doi.org/10.1023/a:1019223515444

Patton, E. G., & Finnigan, J. J. (2013). Canopy turbulence. In H. J. Fernando (Ed.), *Handbook of environmental fluid dynamics* (Vol. 1, pp. 311–327). CRC Press/Taylor & Francis Group.

Patton, E. G., Sullivan, P. P., Shaw, R. H., Finnigan, J. J., & Weil, J. C. (2016). Atmospheric stability influences on coupled boundary layer and canopy turbulence. *Journal of the Atmospheric Sciences*, *73*(4), 1621–1647. https://doi.org/10.1175/JAS-D-15-0068.1

Plake, D., Sörgel, M., Stella, P., Held, A., & Trebs, I. (2015). Influence of meteorology and anthropogenic pollution on chemical flux divergence of the NO-NO_2-O_3 triad above and within a natural grassland canopy. *Biogeosciences*, *12*(4), 945–959. https://doi.org/10.5194/bg-12-945-2015

Raupach, M. R., Finnigan, J. J., & Brunet, Y. (1996). Coherent eddies and turbulence in vegetation canopies: The mixing-layer analogy. *Boundary-Layer Meteorology*, *78*(3–4), 351–382. https://doi.org/10.1007/BF00120941

Romer, P. S., Duffey, K. C., Wooldridge, P. J., Edgerton, E., Baumann, K., Feiner, P. A., et al. (2018). Effects of temperature-dependent NO_x emissions on continental ozone production. *Atmospheric Chemistry and Physics*, *18*(4), 2601–2614. https://doi.org/10.5194/acp-18-2601-2018

Sandu, A., & Sander, R. (2006). Technical note: Simulating chemical systems in Fortran90 and Matlab with the kinetic PreProcessor KPP-2.1. *Atmospheric Chemistry and Physics*, *6*(1), 187–195. https://doi.org/10.5194/acp-6-187-2006

Schulze, B. C., Wallace, H. W., Flynn, J. H., Lefer, B. L., Erickson, M. H., Jobson, B. T., et al. (2017). Differences in BVOC oxidation and SOA formation above and below the forest canopy. *Atmospheric Chemistry and Physics*, *17*(3), 1805–1828. https://doi.org/10.5194/acp-17-1805-2017

Schumann, U. (1989). Large-eddy simulation of turbulent diffusion with chemical reactions in the convective boundary layer. *Atmospheric Environment*, *23*(8), 1713–1727. https://doi.org/10.1016/0004-6981(89)90056-5

Schwantes, R. H., Emmons, L. K., Orlando, J. J., Barth, M. C., Tyndall, G. S., Hall, S. R., et al. (2020). Comprehensive isoprene and terpene gas-phase chemistry improves simulated surface ozone in the southeastern US. *Atmospheric Chemistry and Physics*, *20*(6), 3739–3776. https://doi.org/10.5194/acp-20-3739-2020

Seco, R., Peñuelas, J., & Filella, I. (2008). Formaldehyde emission and uptake by Mediterranean trees *Quercus ilex* and Pinus halepensis. *Atmospheric Environment*, *42*(34), 7907–7914. https://doi.org/10.1016/j.atmosenv.2008.07.006

Shaw, R. H., & Patton, E. G. (2003). Canopy element influences on resolved- and subgrid-scale energy within a large-eddy simulation. *Agricultural and Forest Meteorology*, *115*(1–2), 5–17. https://doi.org/10.1016/s0168-1923(02)00165-x

Shaw, R. H., & Schumann, U. (1992). Large-eddy simulation of turbulent flow above and within a forest. *Boundary-Layer Meteorology*, *61*(1), 47–64. https://doi.org/10.1007/BF02033994

Sparks, J., Monson, R., Sparks, K., & Lerdau, M. (2001). Leaf uptake of nitrogen dioxide (NO_2) in a tropical wet forest: Implications for tropospheric chemistry. *Oecologia*, *127*(2), 214–221. https://doi.org/10.1007/s004420000594

Steiner, A. L. (2020). Role of the terrestrial biosphere in atmospheric chemistry and climate. *Accounts of Chemical Research*, *53*(7), 1260–1268. https://doi.org/10.1021/acs.accounts.0c00116

Stella, P., Loubet, B., de Berranger, C., Charrier, X., Ceschia, E., Gerosa, G., et al. (2019). Soil ozone deposition: Dependence of soil resistance to soil texture. *Atmospheric Environment*, *199*, 202–209. https://doi.org/10.1016/j.atmosenv.2018.11.036

Su, H.-B., Shaw, R. H., Paw, U. K. T., Moeng, C.-H., & Sullivan, P. P. (1998). Turbulent statistics of neutrally stratified flow within and above a sparse forest from large-eddy simulation and field observations. *Boundary-Layer Meteorology*, *88*(3), 363–397. https://doi.org/10.1023/a:1001108411184

Su, L., Patton, E. G., Vilà-Guerau de Arellano, J., Guenther, A. B., Kaser, L., Yuan, B., et al. (2016). Understanding isoprene photooxidation using observations and modeling over a subtropical forest in the southeastern US. *Atmospheric Chemistry and Physics*, *16*(12), 7725–7741. https://doi.org/10.5194/acp-16-7725-2016

Sullivan, P. P., McWilliams, J. C., & Moeng, C.-H. (1996). A grid nesting method for large-eddy simulation of planetary boundary-layer flows. *Boundary-Layer Meteorology*, *80*(1–2), 167–202. https://doi.org/10.1007/bf00119016

Sullivan, P. P., & Patton, E. G. (2011). The effect of Mesh resolution on convective boundary layer statistics and structures generated by large-eddy simulation. *Journal of the Atmospheric Sciences*, *68*(10), 2395–2415. https://doi.org/10.1175/jas-d-10-05010.1

Sun, S., Moravek, A., Trebs, I., Kesselmeier, J., & Sörgel, M. (2016). Investigation of the influence of liquid surface films on O_3 and PAN deposition to plant leaves coated with organic/inorganic solution. *Journal of Geophysical Research: Atmospheres*, *121*(23), 14239–14256. https://doi.org/10.1002/2016JD025519

Sykes, R. I., Henn, D. S., Parker, S. F., & Lewellen, W. S. (1992). Large-eddy simulation of a turbulent reacting plume. *Atmospheric Environment, Part A: General Topics*, *26*(14), 2565–2574. https://doi.org/10.1016/0960-1686(92)90109-x

Sykes, R. I., Parker, S. F., Henn, D. S., & Lewellen, W. S. (1994). Turbulent mixing with chemical reaction in the planetary boundary layer. *Journal of Applied Meteorology*, *33*(7), 825–834. https://doi.org/10.1175/1520-0450(1994)033<0825:tmwcri>2.0.co;2

Thornton, F. C., Pier, P. A., & Valente, R. J. (1997). NO emissions from soils in the southeastern United States. *Journal of Geophysical Research*, *102*(D17), 21189–21195. https://doi.org/10.1029/97JD01567

Trainer, M., Williams, E. J., Parrish, D. D., Buhr, M. P., Allwine, E. J., Westberg, H. H., et al. (1987). Models and observations of the impact of natural hydrocarbons on rural ozone. *Nature*, *329*(6141), 705–707. https://doi.org/10.1038/329705a0

Travis, K. R., Jacob, D. J., Fisher, J. A., Kim, P. S., Marais, E. A., Zhu, L., et al. (2016). Why do models overestimate surface ozone in the Southeast United States? *Atmospheric Chemistry and Physics*, *16*(21), 13561–13577. https://doi.org/10.5194/acp-16-13561-2016

Trowbridge, A. M., Stoy, P. C., & Phillips, R. P. (2020). Soil biogenic volatile organic compound flux in a mixed hardwood forest: Net uptake at warmer temperatures and the importance of mycorrhizal associations. *Journal of Geophysical Research: Biogeosciences*, *124*(4), e2019JG005479. https://doi.org/10.1029/2019JG005479

Turnipseed, A. A., Burns, S. P., Moore, D. J., Hu, J., Guenther, A. B., & Monson, R. K. (2009). Controls over ozone deposition to a high elevation subalpine forest. *Agricultural and Forest Meteorology*, *149*(9), 1447–1459. https://doi.org/10.1016/j.agrformet.2009.04.001

Valente, R. J., & Thornton, F. C. (1993). Emissions of NO from soil at a rural site in central Tennessee. *Journal of Geophysical Research*, *98*(D9), 16745–16753. https://doi.org/10.1029/93JD01417

Vilà-Guerau de Arellano, J., Kim, S.-W., Barth, M. C., & Patton, E. G. (2005). Transport and chemical transformations influenced by shallow cumulus over land. *Atmospheric Chemistry and Physics*, *5*(12), 3219–3231. https://doi.org/10.5194/acp-5-3219-2005

Wang, D., Hinckley, T. M., Cumming, A. B., & Braatne, J. (1995). A comparison of measured and modeled ozone uptake into plant leaves. *Environmental Pollution*, *89*(3), 347–254. https://doi.org/10.1016/0269-7491(94)00078-R

Wang, S., Coggon, M. M., Gkatzelis, G. I., Warneke, C., Bourgeois, I., Ryerson, T., et al. (2021). Chemical tomography in a Fresh Wildland fire plume: A large eddy simulation (LES) study. *Journal of Geophysical Research: Atmospheres*, *126*(18), e2021JD035203. https://doi.org/10.1029/2021JD035203

Wang, S., McNamara, S. M., Moore, C. W., Obrist, D., Steffen, A., Shepson, P. B., et al. (2019). Direct detection of atmospheric atomic bromine leading to mercury and ozone depletion. *Proceedings of the National Academy of Sciences*, *116*(29), 14479–14484. https://doi.org/10.1073/pnas.1900613116

Wang, S., & Pratt, K. A. (2017). Molecular halogens above the Arctic snowpack: Emissions, diurnal variations, and recycling mechanisms. *Journal of Geophysical Research: Atmospheres*, *122*(21), 11991–12007. https://doi.org/10.1002/2017JD027175

Wang, W., Ganzeveld, L., Rossabi, S., Hueber, J., & Helmig, D. (2020). Measurement report: Leaf-scale gas exchange of atmospheric reactive trace species (NO_2, NO, O_3) at a northern hardwood forest in Michigan. *Atmospheric Chemistry and Physics*, *20*(19), 11287–11304. https://doi.org/10.5194/acp-20-11287-2020

Weckwerth, T. M., Wilson, J. W., Wakimoto, R. M., & Crook, N. A. (1997). Horizontal convective rolls: Determining the environmental conditions supporting their existence and characteristics. *Monthly Weather Review*, *125*(4), 505–526. https://doi.org/10.1175/1520-0493(1997)125<0505:hcrdte>2.0.co;2

Wei, D., Alwe, H. D., Millet, D. B., Bottorff, B., Lew, M., Stevens, P. S., et al. (2021). FORest Canopy Atmosphere Transfer (FORCAsT) 2.0: Model updates and evaluation with observations at a mixed forest site. *Geoscientific Model Development*, *14*(10), 6309–6329. https://doi.org/10.5194/gmd-14-6309-2021

Wei, D., Alwe, H. D., Millet, D. B., Kavassalis, S. C., Lew, M., Bottorff, B., et al. (2020). Investigation of isoprene dynamics during the day-to-night transition period. *Journal of Geophysical Research: Atmospheres*, *125*(20), e2020JD032784. https://doi.org/10.1029/2020JD032784

Wennberg, P. O., Bates, K. H., Crounse, J. D., Dodson, L. G., McVay, R. C., Mertens, L. A., et al. (2018). Gas-phase reactions of isoprene and its major oxidation products. *Chemical Reviews*, *118*(7), 3337–3390. https://doi.org/10.1021/acs.chemrev.7b00439

Wesely, M. L. (1989). Parameterization of surface resistances to gaseous dry deposition in regional-scale numerical models. *Atmospheric Environment*, *23*(6), 1293–1304. https://doi.org/10.1016/0004-6981(89)90153-4

Wesely, M. L., & Hicks, B. B. (2000). A review of the current status of knowledge on dry deposition. *Atmospheric Environment*, *34*(12–14), 2261–2282. https://doi.org/10.1016/s1352-2310(99)00467-7

Williams, E. J., & Fehsenfeld, F. C. (1991). Measurement of soil nitrogen oxide emissions at three North American ecosystems. *Journal of Geophysical Research*, *96*(D1), 1033–1042. https://doi.org/10.1029/90jd01903

Wolfe, G. M., & Thornton, J. A. (2011). The chemistry of atmosphere-forest exchange (CAFE) model—Part 1: Model description and characterization. *Atmospheric Chemistry and Physics*, *11*(1), 77–101. https://doi.org/10.5194/acp-11-77-2011

Wolfe, G. M., Thornton, J. A., Bouvier-Brown, N. C., Goldstein, A. H., Park, J.-H., McKay, M., et al. (2011). The chemistry of atmosphere-forest exchange (CAFE) model—Part 2: Application to BEARPEX-2007 observations. *Atmospheric Chemistry and Physics*, *11*(3), 1269–1294. https://doi.org/10.5194/acp-11-1269-2011

Wu, Z., Schwede, D. B., Vet, R., Walker, J. T., Shaw, M., Staebler, R., & Zhang, L. (2018). Evaluation and intercomparison of five North American dry deposition algorithms at a mixed forest site. *Journal of Advances in Modeling Earth Systems*, *10*(7), 1571–1586. https://doi.org/10.1029/2017MS001231

Yienger, J. J., & Levy, H., II (1995). Empirical model of global soil-biogenic NO_x emissions. *Journal of Geophysical Research*, *100*(D6), 11447–11464. https://doi.org/10.1029/95JD00370

Zhang, L., Moran, M. D., Makar, P. A., Brook, J. R., & Gong, S. (2002). Modelling gaseous dry deposition in AURAMS: A unified regional air-quality modelling system. *Atmospheric Environment*, *36*(3), 537–560. https://doi.org/10.1016/s1352-2310(01)00447-2